

THREE-DIMENSIONAL GRMHD SIMULATIONS OF NEUTRINO-COOLED ACCRETION DISKS FROM NEUTRON STAR MERGERS

DANIEL M. SIEGEL^{1,*} AND BRIAN D. METZGER¹

¹*Department of Physics and Columbia Astrophysics Laboratory, Columbia University, New York, NY 10027, USA*

(Dated: June 26, 2018)

ABSTRACT

Merging binaries consisting of two neutron stars (NSs) or an NS and a stellar-mass black hole typically form a massive accretion torus around the remnant black hole or long-lived NS. Outflows from these neutrino-cooled accretion disks represent an important site for r -process nucleosynthesis and the generation of kilonovae. We present the first three-dimensional, general-relativistic magnetohydrodynamic (GRMHD) simulations including weak interactions and a realistic equation of state of such accretion disks over viscous timescales (380 ms). We witness the emergence of steady-state MHD turbulence, a magnetic dynamo with an ~ 20 ms cycle, and the generation of a ‘hot’ disk corona that launches powerful thermal outflows aided by the energy released as free nucleons recombine into α -particles. We identify a self-regulation mechanism that keeps the midplane electron fraction low ($Y_e \sim 0.1$) over viscous timescales. This neutron-rich reservoir, in turn, feeds outflows that retain a sufficiently low value of $Y_e \approx 0.2$ to robustly synthesize third-peak r -process elements. The quasi-spherical outflows are projected to unbind 40% of the initial disk mass with typical asymptotic escape velocities of $0.1c$, and may thus represent the dominant mass ejection mechanism in NS–NS mergers. Including neutrino absorption, our findings agree with previous hydrodynamical α -disk simulations that the entire range of r -process nuclei from the first to the third r -process peak can be synthesized in the outflows, in good agreement with observed solar system abundances. The asymptotic escape velocities and the quantity of ejecta, when extrapolated to moderately higher disk masses, are consistent with those needed to explain the red kilonova emission following the NS merger GW170817.

arXiv:1711.00868v2 [astro-ph.HE] 24 Jun 2018

* NASA Einstein Fellow

1. INTRODUCTION

When a binary system consisting of two neutron stars (NSs) or an NS and a rapidly spinning stellar-mass black hole (BH) merges into a single compact object following a prolonged inspiral driven by gravitational-wave (GW) radiation, the outcome is a violent interaction that releases mass and energy into the surrounding environment (Lee & Ramirez-Ruiz 2007; Lehner & Pretorius 2014; Baiotti & Rezzolla 2017). Neutron-rich matter ejected into space during this process subsequently synthesizes elements much heavier than iron via the rapid capture of neutrons onto nuclei (r -process; Lattimer & Schramm 1974; Symbalisty & Schramm 1982; Freiburghaus et al. 1999; Goriely et al. 2011). The highest-mass nuclei reached by the r -process depends on the neutron abundance in the ejecta, as quantified by its electron fraction $Y_e = n_p/n_b$, where n_p and n_b are the proton and total baryon densities, respectively. Exclusively light r -process nuclei with atomic mass $A \lesssim 140$ are created for $0.25 \lesssim Y_e \lesssim 0.40$, while heavier isotopes with $A \gtrsim 140$ are also produced if the ejecta is sufficiently neutron-rich, $Y_e \lesssim 0.25$ (Lippuner & Roberts 2015).

The first detection of GWs from an NS–NS merger (the LIGO Scientific Collaboration & the Virgo Collaboration 2017) and the subsequent localization of this event—dubbed GW170817—to a galaxy at a distance of only ≈ 40 Mpc (e.g. Abbott et al. 2017 and references therein) provides a golden opportunity to test theoretical predictions for the electromagnetic and nucleosynthetic signatures of these events. Eleven hours after the merger, an optical counterpart was discovered (Coulter et al. 2017; Soares-Santos et al. 2017; Valenti et al. 2017; Arcavi et al. 2017; Lipunov et al. 2017; Evans et al. 2017) with a luminosity, thermal spectrum, and rapid temporal decay consistent with “kilonova” (KN) emission powered by the radioactive decay of r -process nuclei synthesized in the merger ejecta (Li & Paczyński 1998; Metzger et al. 2010b; Metzger 2017). Visual (“blue”) KN emission (Metzger et al. 2010b) was detected at early times, which then faded and was supplanted after a few days by a second distinct emission component at near-infrared (“red”) wavelengths (Barnes & Kasen 2013; Tanaka & Hotokezaka 2013; Wollaeger et al. 2017), thus implicating the presence of at least two separate ejecta components. The blue KN is well-modeled as being powered by $\approx 1.5 \times 10^{-2} M_\odot$ of light r -process nuclei (ejecta with an initial electron fraction $Y_e \gtrsim 0.25$) moving at high velocities $\approx 0.2 - 0.3c$, while the red KN requires a greater quantity $\approx 4 \times 10^{-2} M_\odot$ of ejecta that also contains heavy r -process nuclei ($Y_e \lesssim 0.25$) expanding at a lower velocity $v \approx 0.1c$ (e.g. Kasen et al. 2017; Cowperthwaite et al. 2017; Tanvir et al. 2017; Shappee et al. 2017; Kilpatrick et al. 2017; Kasliwal et al. 2017; Nicholl et al. 2017; Chornock et al. 2017; Drout et al. 2017; Mc-

Cully et al. 2017; Tanvir et al. 2017; Villar et al. 2017; however, see Smartt et al. 2017; Tanaka et al. 2017).

Theoretical work has identified several processes that are expected to contribute to mass ejection in NS–NS/NS–BH mergers (e.g. Fernández & Metzger 2016, for a review). Strong tidal forces between the compact objects just prior to their coalescence eject low- Y_e matter focused into the equatorial binary plane (e.g. Rosswog et al. 1999; Oechslin & Janka 2006; Hotokezaka et al. 2013b; Radice et al. 2016; Bovard et al. 2017). However, the total ejecta mass $\approx 5 \times 10^{-2} M_\odot$ inferred for GW170817 exceeds the dynamical ejecta obtained by any general-relativistic (GR) NS–NS merger simulation to date (e.g. Shibata et al. 2017); the velocity $v \approx 0.1c$ of the red KN is, furthermore, several times lower than that found by the numerical simulations.

An NS–NS merger, or an NS–BH merger resulting in tidal disruption of the NS outside of the innermost stable circular orbit, also produces a massive rotating torus surrounding the central compact remnant. This accretion torus provides a promising central engine for powering the collimated relativistic jet needed to create a short gamma-ray burst (Narayan et al. 1992; Aloy et al. 2005; Rezzolla et al. 2010; Ruiz et al. 2016). Outflows from the same torus over longer timescales of up to seconds provides another contribution to the r -process and KN emission, in addition to the dynamical ejecta (Metzger et al. 2008a, 2009; Fernández & Metzger 2013; Perego et al. 2014; Just et al. 2015; Fernández et al. 2015). The torus mass found from numerical simulations can be as high as $\approx 0.1 - 0.2 M_\odot$ in an NS–NS merger if the merger remnant goes through a hypermassive neutron star (HMNS) phase¹ prior to forming a BH (e.g. Shibata & Taniguchi 2006; Hotokezaka et al. 2013a). In this case, the red KN emission from GW170817 could be explained if disk winds carry away $\approx 20 - 40\%$ of the total initial torus mass.

The enormous accretion rates achieved after the merger, up to $\gtrsim 1 M_\odot \text{ s}^{-1}$, occur under conditions that are highly optically thick to photons. However, the disk can still be cooled by thermal neutrino emission (Popham et al. 1999; Narayan et al. 2001; Kohri & Mineshige 2002; Di Matteo et al. 2002; Beloborodov 2003; Kohri et al. 2005; Kawanaka & Mineshige 2007; Chen & Beloborodov 2007), a process that affects the lepton number of the disk in addition to its thermodynamics. The high densities and temperatures achieved in the disk midplane enable weak interactions, particularly the capture of electrons and positrons on free nuclei, to alter Y_e from the initial value of the merger debris. The precise equilibrium value to which Y_e is driven depends

¹ The formation of an HMNS in GW170817 is supported indirectly by the high and sustained level of neutrino irradiation needed to explain the luminous blue KN (indicative of a large quantity of high- Y_e polar ejecta).

on the degree of electron/positron degeneracy through the Pauli blocking factors (Beloborodov 2003).

Magnetohydrodynamic (MHD) turbulence, as fed by the magnetorotational instability (MRI; Balbus & Hawley 1992), is expected to drive accretion in a wide variety of astrophysical environments (Balbus & Hawley 1998), including in NS–NS and NS–BH mergers. However, nearly all previous numerical studies of the post-merger accretion flow have been performed under the assumption of hydrodynamics, adopting an effective hydrodynamical α -viscosity (Shakura & Sunyaev 1973) in place of self-consistent MHD turbulence (Fernández & Metzger 2013; Metzger & Fernández 2014; Just et al. 2015; Fernández et al. 2015; ?).² These calculations also generally assume axisymmetry and a pseudo-Newtonian potential to mimic the effects of the GR spacetime.

A properly calibrated α -disk model can capture the evolution of the disk surface density and bulk angular momentum reasonably well. However, in detail, the nature of the hydrodynamical turbulence (convection versus the MRI-driven turbulence) is fundamentally different from that of the MHD case (Balbus & Hawley 2002; Hawley & Balbus 2002). Furthermore, while in α -disks the thermal energy generated by viscosity is locally dissipated in proportion to the gas density, numerical simulations of MHD disks show that a disproportionately large fraction of their “heating” occurs nonlocally through reconnection in low-density coronal regions (Hirose et al. 2006; Jiang et al. 2014a). This novel feature of MHD disks may be important in the context of hyperaccretion flows because the energy released in the disk corona as free nuclei recombine into α -particles plays a significant role in unbinding mass and driving a mass-loaded outflow (MacFadyen et al. 2001).

This paper presents the first three-dimensional, general-relativistic magnetohydrodynamic (GRMHD) simulations of the neutrino-cooled BH accretion disks created following NS–NS and NS–BH mergers. We begin by describing the methodology of the numerical simulations and our implementation of the microphysics (Sect. 2) before discussing the setup of the initial data (Sect. 3). We then provide a detailed description of the disk evolution (Sect. 4), including the generation of MHD turbulence; the evolution and self-regulation of the midplane electron fraction; the generation of unbound outflows; and the properties of the disk neutrino emission. Finally, we describe our calculation of the r -process abundance yields of the disk outflows (Sect. 5). Our results and their immediate implications for the

r -process in compact object mergers were also summarized in a companion Letter (Siegel & Metzger 2017).³

2. ANALYTICAL AND NUMERICAL SETUP

Our simulations of post-merger accretion disks are performed in ideal GRMHD using the open-source `EinsteinToolkit`⁴ (Löffler et al. 2012) with the GRMHD code `GRHydro` (Mösta et al. 2014). Although we employ a fixed background spacetime for computational efficiency in the present simulations, our code can also handle dynamical spacetimes. We use a finite-volume scheme with piecewise parabolic reconstruction (Colella & Woodward 1984), the HLLC Riemann solver (Harten 1983; Einfeldt 1988), and constrained transport (Tóth 2000) to maintain a divergenceless magnetic field. In this section, we focus exclusively on changes to `GRHydro` and features that we have newly implemented for the current simulations. These include weak interactions and approximate neutrino transport via a leakage scheme (Secs. 2.1 and 2.2), a new framework and methods for the recovery of primitive variables that support composition-dependent equations of state (EOS; Sec. 2.3), and the Helmholtz EOS as a microphysical EOS also valid at comparatively low densities and temperatures to accurately describe the properties of disk outflows (Sec. 2.4).

2.1. GRMHD with weak interactions

The equations of ideal GRMHD with weak interactions include energy and momentum conservation, baryon number conservation, lepton number conservation, and Maxwell’s equations,

$$\nabla_{\mu} T^{\mu\nu} = Qu^{\nu}, \quad (1)$$

$$\nabla_{\mu} (n_{\text{b}} u^{\mu}) = 0, \quad (2)$$

$$\nabla_{\mu} (n_{\text{e}} u^{\mu}) = R, \quad (3)$$

$$\nabla_{\nu} F^{*\mu\nu} = 0, \quad (4)$$

where

$$T^{\mu\nu} = (\rho h + b^2) u^{\mu} u^{\nu} + \left(p + \frac{b^2}{2} \right) g^{\mu\nu} - b^{\mu} b^{\nu}, \quad (5)$$

is the energy-momentum tensor, u^{μ} is the four-velocity, n_{b} is the baryon number density, n_{e} is the electron number density, and $F^{*\mu\nu}$ is the dual of the Faraday electromagnetic tensor. Furthermore, p is the pressure; $h = 1 + \epsilon + p/\rho$ denotes the specific enthalpy, with ϵ being the specific internal energy; $b^{\mu} \equiv (4\pi)^{-1/2} F^{*\mu\nu} u_{\nu}$ is the magnetic field vector in the frame comoving with the

² With the exception of the two-dimensional simulations of Shibata et al. (2007); however, the antidynamo theorem (Cowling 1933) prevents saturated steady-state MHD turbulence in axisymmetry.

³ During the preparation of the present manuscript, Nouri et al. (2017) presented evolution of a magnetized, neutrino-cooled accretion disk from a BH–NS merger over ≈ 60 ms.

⁴ <http://einsteintoolkit.org>

fluid; $b^2 \equiv b^\mu b_\mu$; and $g_{\mu\nu}$ is the space-time metric.⁵ We assume that the thermodynamic properties of matter can be described by a finite-temperature, composition-dependent (three-parameter) EOS formulated as a function of density $\rho = n_b m_b$, where m_b denotes the baryon mass; temperature T ; and electron fraction $Y_e = n_e n_b^{-1}$. The evolution of Y_e is described by Eq. (3). The source terms Qu^ν and R on the right-hand side of Eqs. (1) and (3) account for the evolution of Y_e due to weak interactions, which create neutrinos and antineutrinos that carry away energy and momentum from the system.

For numerical evolution, Eqs. (1)–(4) can essentially be transformed into a set of conservation equations in flat space by adopting a 3+1 split of spacetime into non-intersecting space-like hypersurfaces of constant coordinate time t (Lichnerowicz 1944; Arnowitt et al. 2008), in which case, the line element can be written as

$$ds^2 = -\alpha^2 dt^2 + \gamma_{ij}(dx^i + \beta^i dt)(dx^j + \beta^j dt), \quad (6)$$

where α denotes the lapse function, β^i is the shift vector, and γ_{ij} is the metric induced on every spatial hypersurface. The hypersurfaces are characterized by the time-like unit normal $n^\mu = (\alpha^{-1}, -\alpha^{-1}\beta^i)$ ($n_\mu = (-\alpha, 0, 0, 0)$), which also defines the Eulerian observer, i.e., the observer moving through spacetime with four-velocity n^μ perpendicular to the hypersurfaces. Equations (1)–(4) can then be written as

$$\partial_t(\sqrt{\gamma}\mathbf{q}) + \partial_i[\alpha\sqrt{\gamma}\mathbf{f}^{(i)}(\mathbf{p}, \mathbf{q})] = \alpha\sqrt{\gamma}\mathbf{s}(\mathbf{p}), \quad (7)$$

where γ is the determinant of the spatial metric γ_{ij} and

$$\mathbf{q} \equiv [D, S_i, \tau, B^i, DY_e] \quad (8)$$

denotes the vector of conserved variables. The latter is composed of the conserved density, the conserved momenta, and the conserved energy, defined as

$$D \equiv \rho W, \quad (9)$$

$$S_i \equiv -n_\mu T^\mu_i = \alpha T^0_i = (\rho h + b^2)W^2 v_i - \alpha b^0 b_i, \quad (10)$$

$$\tau \equiv n_\mu n_\nu T^{\mu\nu} - D \quad (11)$$

$$= (\rho h + b^2)W^2 - \left(p + \frac{b^2}{2}\right) - \alpha^2 (b^0)^2 - D, \quad (12)$$

respectively, the three-vector components of the magnetic field $B^\mu \equiv (4\pi)^{-1/2} F^{*\mu\nu} n_\nu$ as measured by the Eulerian observer, as well as the conserved electron fraction DY_e . The Eulerian three-velocity is defined by

$$v^i \equiv \frac{\gamma^i_\mu u^\mu}{-u^\mu n_\mu} = \frac{u^i}{W} + \frac{\beta^i}{\alpha}, \quad v_i = \frac{\gamma_{i\mu} u^\mu}{-u^\mu n_\mu} = \frac{u_i}{W}, \quad (13)$$

where

$$W \equiv -u^\mu n_\mu = \alpha u^0 = \frac{1}{\sqrt{1-v^2}} \quad (14)$$

⁵ In this paper, Greek indices take space-time values 0–3, whereas Roman indices represent the spatial components 1–3 only. Repeated indices are summed over.

denotes the relative Lorentz factor between u^μ and n^μ , with $v^2 \equiv \gamma_{ij} v^i v^j$. For completeness, the comoving and Eulerian magnetic field components are related by

$$b^i = \frac{B^i}{W} + b^0(\alpha v^i - \beta^i), \quad b_i = \frac{B_i}{W} + \alpha b^0 v_i \quad (15)$$

and

$$b^0 = \frac{W}{\alpha} B^i v_i, \quad b^2 = b^\mu b_\mu = \frac{B^2 + (\alpha b^0)^2}{W^2}, \quad (16)$$

where $B^2 \equiv B^i B_i$. Furthermore,

$$\mathbf{p} \equiv [\rho, v^i, \epsilon, B^i, Y_e] \quad (17)$$

summarizes the set of primitive variables. The fluxes are given by

$$\mathbf{f}^{(i)}(\mathbf{p}, \mathbf{q}) \equiv \begin{bmatrix} D\tilde{v}^i \\ S_j \tilde{v}^i + \left(p + \frac{b^2}{2}\right) \delta_j^i - \frac{B^i}{W} b_j \\ \tau \tilde{v}^i + \left(p + \frac{b^2}{2}\right) v^i - \alpha b^0 \frac{B^i}{W} \\ \tilde{v}^i B^k - \tilde{v}^k B^i \\ DY_e \tilde{v}^i \end{bmatrix} \quad (18)$$

and the sources by

$$\mathbf{s}(\mathbf{p}) \equiv \begin{bmatrix} 0 \\ T^{\mu\nu}(\partial_\mu g_{j\nu} - \Gamma_{\nu\mu}^\delta g_{\delta j}) + WQv_j \\ \alpha(T^{0\mu} \partial_\mu \ln \alpha - T^{\mu\nu} \Gamma_{\mu\nu}^0) + WQ \\ 0^k \\ Rm_b \end{bmatrix}, \quad (19)$$

where $\tilde{v}^i \equiv v^i - \beta^i \alpha^{-1}$, and $\Gamma_{\beta\gamma}^\alpha$ are the Christoffel symbols constructed from $g_{\mu\nu}$.

2.2. Neutrino leakage scheme

Weak interactions and neutrino transport determine the source terms on the right-hand side of Eqs. (1) and (3), and the terms apart from the geometrical source terms in Eq. (7) (cf. Eq. (19)). For the present simulations, we employ an energy-averaged (gray) leakage scheme, which we have newly implemented into GRHydro. Such leakage schemes are widely used in both core-collapse supernova and compact-binary merger simulations (e.g., van Riper & Lattimer 1981; Ruffert et al. 1996; Rosswog & Liebendörfer 2003; Sekiguchi et al. 2011; Ott et al. 2013; Radice et al. 2016; Perego et al. 2016). Our implementation closely follows the one by Radice et al. (2016), which is based on Galeazzi et al. (2013), which, in turn, builds on Ruffert et al. (1996) and Bruenn (1985). We follow the procedure discussed in Neilsen et al. (2014) to compute optical depths, which is well suited for aspherical and complex

geometries (such as that of an accretion disk). In the following, we briefly outline some aspects of our leakage scheme.

We specify the net neutrino heating/cooling rate per unit volume in the rest frame of the fluid, Q , and the net lepton emission/absorption rate per unit volume in the rest frame of the fluid, R , (cf. Eqs. (1),(3), and (19)) as a local balance of absorption and emission of free-streaming neutrinos,

$$R = \sum_{\nu_i} \kappa_{\nu_i} n_{\nu_i} - (R_{\nu_e}^{\text{eff}} - R_{\bar{\nu}_e}^{\text{eff}}) \quad (20)$$

and

$$Q = \sum_{\nu_i} \kappa_{\nu_i} n_{\nu_i} E_{\nu_i} - \sum_{\nu_i} Q_{\nu_i}^{\text{eff}}. \quad (21)$$

Here $\nu_i = \{\nu_e, \bar{\nu}_e, \nu_x\}$, where ν_e denotes electron neutrinos, $\bar{\nu}_e$ denotes electron antineutrinos, and the heavy-lepton neutrinos ν_μ and ν_τ are collectively labeled as ν_x . Furthermore, κ_{ν_i} , n_{ν_i} , and E_{ν_i} , denote the corresponding absorption opacities, number densities, and mean energies of the free-streaming neutrinos in the rest frame of the fluid, respectively. Finally, $R_{\nu_e}^{\text{eff}}$, $R_{\bar{\nu}_e}^{\text{eff}}$, and $Q_{\nu_i}^{\text{eff}}$, denote the corresponding effective number and energy emissivities in the rest frame of the fluid. For the present simulations, we neglect neutrino absorption, as the accretion disk simulated here remains optically thin to all neutrino species at all times (cf. Siegel & Metzger 2017). Neutrino absorption is only expected to appreciably change the outflow and disk dynamics for significantly more massive accretion disks (Fernández & Metzger 2013).

The effective emission/cooling rates $R_{\nu_i}^{\text{eff}}$ and $Q_{\nu_i}^{\text{eff}}$ take effects of finite optical depth into account and are computed from the intrinsic (free) emission rates R_{ν_i} and Q_{ν_i} by (cf. Eq. (B22) and (B23) of Ruffert et al. 1996)

$$R_{\nu_i}^{\text{eff}} = \frac{R_{\nu_i}}{1 + \frac{t_{\text{diff},\nu_i}}{t_{\nu_i}^{\text{em},R}}}, \quad Q_{\nu_i}^{\text{eff}} = \frac{Q_{\nu_i}}{1 + \frac{t_{\text{diff},\nu_i}}{t_{\nu_i}^{\text{em},Q}}}. \quad (22)$$

Here

$$t_{\text{diff},\nu_i} = D_{\text{diff}} \kappa_{\nu_i}^{-1} \tau_{\nu_i}^2 \quad (23)$$

denote the local diffusion timescales, where τ_{ν_i} are the corresponding optical depths (see below), and D_{diff} is a diffusion normalization factor, which we set to $D_{\text{diff}} = 6$ (O'Connor & Ott 2010). Furthermore,

$$t_{\nu_i}^{\text{em},R} = \frac{R_{\nu_i}}{n_{\nu_i}}, \quad t_{\nu_i}^{\text{em},Q} = \frac{Q_{\nu_i}}{e_{\nu_i}} \quad (24)$$

are the local neutrino number and energy emission timescales, where e_{ν_i} refers to the neutrino energy densities and

$$R_{\nu_i} = \delta_{\nu_i,\nu_e} R_{\nu_e}^\beta + \delta_{\nu_i,\bar{\nu}_e} R_{\bar{\nu}_e}^\beta + R_{\nu_i}^{\text{ee}} + R_{\nu_i}^\gamma, \quad (25)$$

$$Q_{\nu_i} = \delta_{\nu_i,\nu_e} Q_{\nu_e}^\beta + \delta_{\nu_i,\bar{\nu}_e} Q_{\bar{\nu}_e}^\beta + Q_{\nu_i}^{\text{ee}} + Q_{\nu_i}^\gamma \quad (26)$$

(cf. Eqs. (B18)–(B21) of Ruffert et al. 1996). The emission rates $R_{\nu_i}^\beta$ and $Q_{\nu_i}^\beta$, $R_{\nu_i}^{\text{ee}}$ and $Q_{\nu_i}^{\text{ee}}$, and $R_{\nu_i}^\gamma$ and $Q_{\nu_i}^\gamma$ are computed as in Galeazzi et al. (2013) and reflect the contributing neutrino mechanisms we consider. These are, respectively,

- (i) charged current β -processes,

$$e^- + p \rightarrow n + \nu_e, \quad (27)$$

$$e^+ + n \rightarrow p + \bar{\nu}_e, \quad (28)$$

the strongest neutrino emission mechanism in hot and dense nuclear matter;

- (ii) electron-positron pair annihilation,

$$e^- + e^+ \rightarrow \nu_e + \bar{\nu}_e, \quad (29)$$

$$e^- + e^+ \rightarrow \nu_x + \bar{\nu}_x, \quad (30)$$

which is most relevant in nondegenerate nuclear matter at low densities and high temperatures; and

- (iii) plasmon decay,

$$\gamma \rightarrow \nu_e + \bar{\nu}_e, \quad (31)$$

$$\gamma \rightarrow \nu_x + \bar{\nu}_x, \quad (32)$$

which is efficient at intermediate densities and high temperatures.

2.2.1. Calculation of opacities

The neutrino opacities κ_{ν_i} introduced above may be subdivided into contributions from absorption and scattering,

$$\kappa_{\nu_i} = \kappa_{\nu_i,\text{abs}} + \kappa_{\nu_i,\text{scat}}, \quad (33)$$

where

- (i) $\kappa_{\nu_i,\text{abs}}$ refers to absorption of electron and anti-electron neutrinos only,

$$\nu_e + n \rightarrow p + e^-, \quad (34)$$

$$\bar{\nu}_e + p \rightarrow n + e^+; \quad (35)$$

and

- (ii) $\kappa_{\nu_i,\text{scat}}$ refers to coherent scattering on heavy nuclei A and scattering on free nucleons,

$$\nu_i + A \rightarrow \nu_i + A, \quad (36)$$

$$\bar{\nu}_i + A \rightarrow \bar{\nu}_i + A, \quad (37)$$

$$\nu_i + [n, p] \rightarrow \nu_i + [n, p], \quad (38)$$

$$\bar{\nu}_i + [n, p] \rightarrow \bar{\nu}_i + [n, p]. \quad (39)$$

The absorption and scattering opacities for these processes are computed as in Galeazzi et al. (2013).

2.2.2. Calculation of optical depths

We reduce the nonlocal computation of optical depths τ_{ν_i} to an effective local problem by applying the method described in Neilsen et al. (2014), which is well suited for aspherical geometries such as an accretion disk. Global integrations are avoided by decomposing the optical depth at a given grid point into the optical depth to any neighboring point plus the already computed optical depth $\tau_{\nu_i, \text{neigh}}$ at the neighboring point, which we compute as

$$\tau_{\nu_i, \text{neigh}} + \bar{\kappa}_{\nu_i} (\bar{\gamma}_{ab} dx^a dx^b)^{1/2}, \quad (40)$$

where dx^a is the spatial coordinate distance vector between the two points, and $\bar{\kappa}_{\nu_i}$ and $\bar{\gamma}_{ab}$ denote the opacities and components of the spatial metric averaged between the two neighboring points. We define the optical depth at a given grid point as the minimum over all expressions (Equation (40)) computed for all neighboring points.

2.3. Recovery of primitive variables

Conservative GRMHD schemes evolve the conserved variables \mathbf{q} (cf. Eq. (7)). This involves computing the flux terms $\mathbf{f}^{(i)}(\mathbf{p}, \mathbf{q})$ and source terms $\mathbf{s}(\mathbf{p})$ for a given \mathbf{q} , which requires us to obtain the primitive variables \mathbf{p} from the conserved ones. While the conservative variables as a function of primitive variables, $\mathbf{q} = \mathbf{q}(\mathbf{p})$, are given in analytic form by Eqs. (9)–(16), the inverse relation, $\mathbf{p} = \mathbf{p}(\mathbf{q})$, i.e., the recovery of primitive variables from conservative ones, is not known in closed form; this instead requires numerical inversion of the aforementioned set of nonlinear equations.

We have implemented a new framework for the recovery of primitive variables in `GRHydro` that provides support for any composition-dependent, finite-temperature (three-parameter) EOS, as well as a recovery scheme based on a three-dimensional Newton–Raphson solver using Eqs. (21), (22), and (28) in Cerdá-Durán et al. (2008). We find that this scheme has particularly fast convergence properties as compared to other schemes, typically involving a minimum of EOS calls (Siegel et al. 2018; Siegel & Mösta 2018⁶). The latter fact is of particular importance for three-parameter EOS, as most such EOSs are provided in the form of multidimensional tables, and table lookups can become computationally expensive. Furthermore, its ability to recover strongly magnetized regions is important for evolving low-density magnetized disk winds, as in the present simulation.

2.4. Helmholtz EOS

We base the microphysical description of matter at the relatively low densities and temperatures of our present simulation on the Helmholtz EOS (Timmes &

Arnett 1999; Timmes & Swesty 2000), which we have newly implemented into `GRHydro`. Nuclear-reaction networks such as `SkyNet` (Lippuner & Roberts 2017), which we employ for calculating r -process abundance yields, also use the Helmholtz EOS, which is how we minimize thermodynamical inconsistencies between the simulation and subsequent postprocessing to obtain nucleosynthesis abundance yields.

The Helmholtz EOS is formulated in terms of a Helmholtz free energy, which takes into account contributions from nuclei (treated as ideal gas) with Coulomb corrections, electrons and positrons with an arbitrary degree of relativity and degeneracy, and photons in local thermodynamic equilibrium. As nuclei in the present simulation, we consider free neutrons and protons, as well as α -particles. We have modified the Helmholtz EOS to include the nuclear binding energy release from α -particle formation. We compute the abundances of nuclei at given (ρ, T, Y_e) assuming nuclear statistical equilibrium (NSE), i.e., by numerically solving the Saha equation supplemented with baryon number and charge conservation,

$$n_p^2 n_n^2 = 2n_\alpha \left(\frac{m_b k_B T}{2\pi \hbar^2} \right)^{9/2} \exp(-Q_\alpha/k_B T), \quad (41)$$

$$n_b = n_n + n_p + 4n_\alpha, \quad (42)$$

$$n_b Y_e = n_p + 2n_\alpha. \quad (43)$$

Here k_B is the Boltzmann constant, \hbar is the reduced Planck constant, $Q_\alpha \simeq 28.3 \text{ MeV}$ is the nuclear binding energy of an α -particle, and n_n , n_p , and n_α denote the number densities of neutrons, protons, and α -particles, respectively. We also include additional terms to the thermodynamical derivatives that arise from compositional changes with respect to (ρ, T, Y_e) , i.e., from the fact that $\partial n_n / \partial \rho$, $\partial n_n / \partial T$, $\partial n_n / \partial Y_e$ etc. from Eqs. (41)–(43) are nonzero. These additional terms can be important to the evolution code, as, e.g., the Riemann solver can depend on thermodynamic derivatives through the sound speed.

3. INITIAL DATA AND GRID SETUP

We start our long-term disk simulation from an axisymmetric equilibrium torus around a rotating BH of mass $M_{\text{BH}} = 3 M_\odot$ with dimensionless spin $\chi_{\text{BH}} = 0.8$, computed in horizon-penetrating Kerr–Schild coordinates (Kerr 1963). We assume a constant specific angular momentum and a small constant specific entropy of $8 k_B$ per baryon. Under these assumptions, the GR Euler equations reduce to inverting the specific enthalpy given by (Stergioulas 2011; Friedman & Stergioulas 2013)

$$hu_0 = \text{const.}, \quad (44)$$

in order to find all other thermodynamic variables, including density and temperature. Here the right-hand

⁶ Codebase: <https://doi.org/10.5281/zenodo.1213306>

Table 1. Initial data: BH–Torus configuration with (from left to right) BH mass and dimensionless spin, torus mass, radius at maximum density, specific entropy, electron fraction, and maximum magnetic field strength.

M_{BH}	χ_{BH}	M_{t0}	R_0	s_0	Y_{e0}	B_{max}
(M_{\odot})		(M_{\odot})	(km)	(k_{B}/b)		(G)
3.00	0.8	0.03	30	8	0.1	3.3×10^{14}

side is an arbitrary integration constant and u_0 is entirely determined by the metric components of the Kerr–Schild metric. In numerically inverting Eq. (44), we assume a constant initial electron fraction $Y_e = 0.1$ and a torus mass of $M_{t0} = 0.03 M_{\odot}$, with a location of maximum density at $R_0 = 30 \text{ km}$ [$6.7 M_{\text{BH}}$] (see also Tab. 1); the inner and outer radii of the torus are located at $R_{\text{in},0} = 18 \text{ km}$ [$4 M_{\text{BH}}$] and $R_{\text{out},0} = 106 \text{ km}$ [$24 M_{\text{BH}}$].

We endow the equilibrium torus with a weak initial magnetic seed field, confined to the interior of the torus and defined by the vector potential with components $A^r = A^\theta = 0$ and $A^\phi = A_b \max\{p - p_{\text{cut}}, 0\}$. Here $p_{\text{cut}} = 1.3 \times 10^{-2} p_{\text{max}}$, where p_{max} is the pressure at maximum density in the torus; tuning A_b , we set the initial field strength such that the maximum magnetic-to-fluid pressure ratio in the torus is $p_B/p_f < 5 \times 10^{-3}$, where $p_B = b^2/2$; this ratio corresponds to a maximum initial magnetic field strength of $3.3 \times 10^{14} \text{ G}$.

The initial parameters of the BH and torus correspond to those of a typical NS merger remnant. The BH spins resulting from NS–NS mergers leading to prompt BH formation are typically $\chi_{\text{BH}} \approx 0.8$ (Kiuchi et al. 2009; Rezzolla et al. 2010; Bernuzzi et al. 2014) and cannot be significantly larger (Kastaun et al. 2013); the case of delayed BH formation is typically not much smaller, $\chi_{\text{BH}} \lesssim 0.7$ (Sekiguchi et al. 2016). Furthermore, $\chi_{\text{BH}} \sim 0.8$ is a reasonable estimate of the spin of the BH in a BH–NS merger in cases when the NS is tidally disrupted and thus able to form a massive torus (Foucart 2012). The initial torus mass we adopt is also fairly typical of NS mergers (e.g., Hotokezaka et al. 2011; Foucart et al. 2017). Furthermore, we have chosen the initial parameters in such a way that (i) the setup is very similar to previous 2D Newtonian simulations (Fernández et al. 2015) and (ii) the resulting configuration after relaxation and having reached a saturated MRI state (see Sec. 4.1) closely resembles the properties of early post-merger accretion disks obtained from magnetized NS–NS merger simulations such as, e.g., Ciolfi et al. (2017).

The initial torus is embedded in a tenuous atmosphere of uniform density $\rho = 37 \text{ g cm}^{-3}$, temperature $T = 10^5 \text{ K}$, and electron fraction $Y_e = 1$. Both the density and temperature of the atmosphere are sufficiently low to influence neither the dynamics nor the composition of the disk outflows. This density value translates into a total atmosphere mass on the entire computa-

tional domain of $6.7 \times 10^{-5} M_{\odot}$ (and $7.8 \times 10^{-8} M_{\odot}$ over the volume with radius 1000 km, at which we evaluate bound vs. unbound outflow), which is safely orders of magnitude smaller than the total ejecta mass in the disk outflows. Furthermore, at $T = 10^5 \text{ K}$, the material is sufficiently cold that weak interactions are completely frozen out.

The computational domain consists of a Cartesian grid hierarchy with the BH at the center, embedded in eight refinement levels extending out to $1.53 \times 10^9 \text{ cm}$ in all coordinate directions. The initial torus is entirely contained by the finest refinement level, which has a diameter of 240 km with a resolution of $\Delta_{xyz} = 856 \text{ m}$, which corresponds to $\Delta_{xyz}/M_{\text{BH}} \simeq 0.19$. The simulations are performed in full 3D without symmetries.

4. DISK EVOLUTION

A brief description of the disk evolution corresponding to the initial data described above was already provided in Siegel & Metzger (2017). Here we present a more detailed analysis of the evolution and address some general properties of neutrino-cooled accretion disks for the first time in GRMHD. In particular, we describe the initial transient phase in which we witness the onset of MHD turbulence and describe how a steady turbulent state is achieved (Sec. 4.1); we demonstrate the existence of a self-regulation mechanism to mild electron degeneracy in the inner parts of the disk, which ensures neutron-rich outflows and the production of third-peak r -process elements (Sec. 4.3); and we present direct evidence for a fully operational magnetic dynamo in the disk in the presence of neutrino cooling and discuss the physical processes that generate winds in the hot disk corona (Sec. 4.4). Finally, we discuss the global structure and long-term evolution of the disk (Sec. 4.5) and the characteristics of its neutrino radiation (Sec. 4.6).

4.1. Onset of MHD turbulence and its steady state

Magnetic stresses generated by turbulence mediate angular momentum transport and energy dissipation in accretion disks around compact objects. Turbulence is thought to be generated in this context by the MRI, which refers to certain exponentially growing modes that can develop in differentially rotating magnetized fluids (e.g., Velikhov 1959; Chandrasekhar 1960; Balbus & Hawley 1991, 1998; Balbus 2003; Armitage 2011). The MRI is a local instability, the growth of which is dominated by a fastest-growing MRI mode; in GRMHD, its wavelength can be estimated by (Siegel et al. 2013; Kiuchi et al. 2015b, 2017)

$$\lambda_{\text{MRI}} \simeq \frac{2\pi}{\Omega} \frac{b}{\sqrt{4\pi\rho h + b^2}}, \quad (45)$$

where $\Omega = u^\phi/u^0$ is the angular frequency and $b \equiv \sqrt{b^2}$. The MRI is typically well resolved when λ_{MRI} is numerically resolved by at least 10 grid points and partially

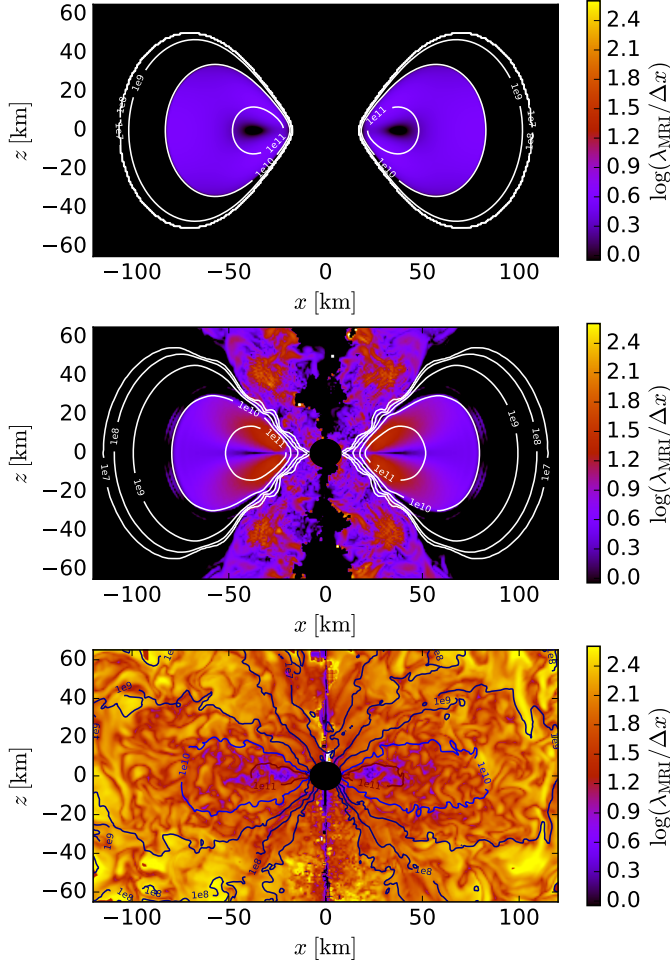


Figure 1. Number of grid points per fastest-growing MRI wavelength λ_{MRI} in the meridional plane at $t = 0$ ms (top), at $t = 1.1$ ms (center), and at $t = 20$ ms (bottom). Also shown are the contours of the rest-mass density at $\rho = [10^7, 10^8, 10^9, 10^{10}, 10^{11}] \text{ g cm}^{-3}$.

resolved with more than ~ 5 grid points (e.g., Siegel et al. 2013; Kiuchi et al. 2015b).

At $t = 0$ ms, λ_{MRI} is only resolved by ~ 5 grid points in the high-density region of the initial torus (cf. Fig. 1, top panel). Within ≈ 1 ms, however, by initial relaxation and magnetic winding, the high-density part ($\sim 10^{10} - 10^{11} \text{ g cm}^{-3}$) of the torus rapidly enters a regime in which λ_{MRI} is resolved by 10 or more grid points (cf. Fig. 1, center panel). Indeed, starting at ≈ 1 ms, we witness the onset of magnetic field amplification in the poloidal field at the expected rate for the MRI $\propto \exp(t/\tau_{\text{MRI}})$, where (Siegel et al. 2013)

$$\tau_{\text{MRI}} \simeq \frac{1}{\Omega} \quad (46)$$

until saturation (cf. Fig. 2, top panel); the onset of the instability leads to a total amplification by roughly 1.5

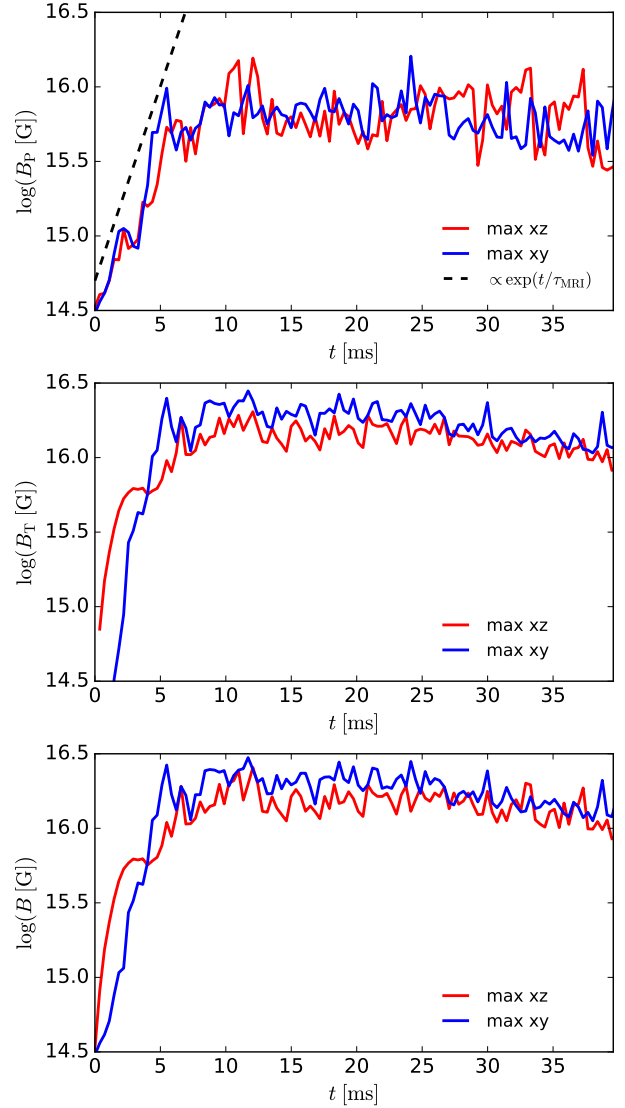


Figure 2. Maximum poloidal (top), toroidal (center), and total (bottom) magnetic field strength in the xy and xz planes during the early transient phase of the disk evolution. The dashed line indicates the expected exponential magnetic field growth due to the MRI for typical parameters at maximum density in the disk.

orders of magnitude for the maximum poloidal magnetic field strength.

As we start with a purely poloidal magnetic field configuration, the toroidal magnetic field component first needs to be amplified by magnetic winding in order for the grid setup to resolve the MRI in the toroidal field. For the maximum toroidal magnetic field strength, this initial amplification process by magnetic winding takes a few ms (Fig. 2, center panel) and slightly longer for other parts of the disk that start with smaller poloidal field strengths. Combined amplification by winding and the MRI leads to an overall increase of almost two or-

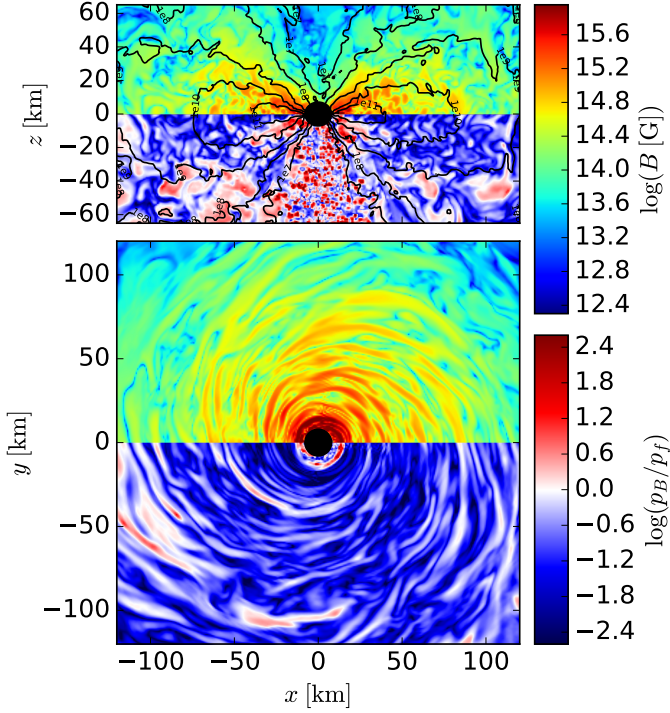


Figure 3. Magnetic field strength B and the magnetic-to-fluid pressure ratio p_B/p_f in the meridional (top) and equatorial (bottom) plane at $t = 20$ ms, when the disk has reached a quasi-stationary state. Contours refer to rest-mass density at $\rho = [10^7, 10^8, 10^9, 10^{10}, 10^{11}] \text{ g cm}^{-3}$.

ders of magnitude in the maximum total magnetic field strength within the first $\approx 5 - 10$ ms (Fig. 2, bottom panel).

By $t = 20$ ms, the disk has reached a quasi-stationary state, in which λ_{MRI} is typically resolved by 10 or more grid points (Fig. 1, bottom panel). The MRI remains resolved in this way throughout the torus for the rest of the simulation, although properly resolving the MRI very close to the BH is a challenging task with current computational resources; close to the BH, we do not resolve the MRI with > 10 grid points at all times and spatial points. However, we do not expect that this appreciably affects our results for the quantity and composition of the disk outflows, since these are typically generated on larger spatial scales (see, e.g., Sec. 4.4).

The quasi-stationary state reached at $t = 20$ ms and depicted in Fig. 1 (bottom panel) and Fig. 3 is very similar to the very early state of accretion disks obtained in recent NS–NS merger simulations. In particular, the typical magnetic field strengths of up to $\sim 10^{15}$ G close to the BH and the disk midplane, as well as the typical magnetic-to-fluid pressure ratios of $\sim 10^{-3} - 10^{-1}$ (cf. Fig. 3), were also obtained by Kiuchi et al. (2015b) and Ciolfi et al. (2017). This state at $t = 20$ ms serves as initial data for the rest of the simulation, and all matter accreted onto the BH or ejected from the disk during the

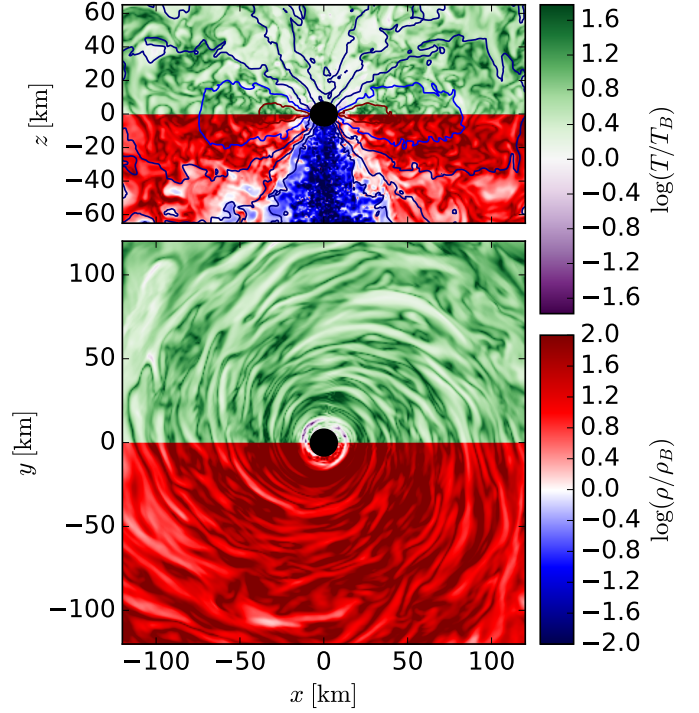


Figure 4. Landau-level quantization: temperature in units of the critical temperature T_B and rest-mass density in units of the critical rest-mass density ρ_B (see text) in the meridional (top) and equatorial (bottom) plane at $t = 20$ ms, when the disk has reached a quasi-stationary state. Also shown are the contours of the rest-mass density at $\rho = [10^7, 10^8, 10^9, 10^{10}, 10^{11}] \text{ g cm}^{-3}$. Since either $\rho \gg \rho_B$ or $T \gtrsim T_B$, the effects of Landau-level quantization are not important.

relaxation phase $t < 20$ ms is discarded from all further analysis.

4.2. Landau-level quantization

Strong magnetic fields $\sim 10^{15} - 10^{16}$ G (cf. Fig. 3) can potentially modify the EOS and the neutrino emission and absorption rates (Eqs. (27)–(30) and (34)–(35)) through the quantization of energy levels for electrons and positrons and their motion perpendicular to the magnetic field (Lai & Qian 1998; Duan & Qian 2004, 2005). Such effects of Landau-level quantization may become relevant for densities below a critical density (Haensel et al. 2007; Harding & Lai 2006; Kiuchi et al. 2015a)

$$\rho_B = 2.23 \times 10^9 \left(\frac{Y_e}{0.1} \right)^{-1} \left(\frac{B}{10^{15} \text{ G}} \right)^{3/2} \text{ g cm}^{-3} \quad (47)$$

and/or below a critical temperature T_B (Harding & Lai 2006)

$$T_B = \begin{cases} \frac{m_e c^2}{k_B} \left(\sqrt{\frac{2B}{B_Q} + 1} - 1 \right), & \rho \leq \rho_B \\ \frac{\hbar \omega_c}{k_B} (1 + x_F^2)^{-1/2}, & \rho \gg \rho_B \end{cases} \quad (48)$$

Here m_e is the electron mass, c is the speed of light, $\omega_c = eB/m_e c$ is the cyclotron frequency, $x_F = \hbar(3\pi^2 Y_e \rho)^{1/3}$ is the normalized relativistic Fermi momentum, and $B_Q = 4.414 \times 10^{13}$ G is the critical QED magnetic field strength.

Figure 4 shows that, typically, $\rho \gg \rho_B$ and $T \gtrsim T_B$ in the disk. Consequently, many Landau levels are populated, and their thermal widths are larger than the level spacing, such that the magnetic field is nonquantizing. In the polar funnel, $\rho \ll \rho_B$, but still $T \gtrsim T_B$, such that, again, the magnetic field has a nonquantizing effect. Since the disk remains in this state throughout the entire simulation, we conclude that the effects of Landau-level quantization are not important for the disk evolution.

4.3. Disk self-regulation

In the neutron-rich environment of the post-merger accretion disk, one might naively expect positron captures onto neutrons, $e^+ + n \rightarrow p + \bar{\nu}_e$ (Eq. (28)), to be favored over electron captures (Eq. (27)), such that the disk matter would protonize over viscous timescales of hundreds of ms, raising the proton/electron fraction Y_e (e.g. Metzger et al. 2009). This effect is indeed evident from Fig. 5 in some portions of the disk. However, a monotonic rise of Y_e in the disk midplane raises the question of how outflows from the disk can remain sufficiently neutron-rich to synthesize heavy r -process elements, even at late times in the disk evolution. As we now describe, the reason is the existence of a self-regulation mechanism in the inner parts of the disk, which keeps a reservoir of neutron-rich material that is continuously fed into the outflows.

Once the disk has reached a quasi-stationary state (cf. Sec. 4.1 and 4.4), it regulates itself to mild electron degeneracy, which, in the presence of optically thin neutrino cooling, results in a low Y_e state ($Y_e \sim 0.1$).⁷ This mechanism has been noted in the context of 1D models of neutrino-cooled accretion disks on analytical and semi-analytical grounds (Kawanaka & Mineshige 2007; Chen & Beloborodov 2007; Metzger et al. 2009), and the first evidence of self-regulation in a full 3D GRMHD simulation has been presented in Siegel & Metzger (2017). Here we elaborate on these results and discuss the mechanism in somewhat more detail; the existence of this mechanism is important for the generation of neutron-rich outflows from the disk (Sec. 4.4), their r -process nucleosynthesis yields (Sec. 5), and the resulting thermal emission (KN).

⁷ For more massive tori than those we consider here, neutrinos can be “trapped” in the flow (such that the neutrino diffusion timescale out of the torus exceeds the accretion timescale), and this can result in a somewhat higher midplane electron fraction than that for disks in which neutrinos are free to escape (e.g. Di Matteo et al. 2002; Beloborodov 2003).

In the hot and dense accretion disk, the number densities of electrons and positrons (e^\pm) in thermodynamic equilibrium with the baryonic matter are given by

$$n_\pm = \frac{(m_e c)^3}{\pi^2 \hbar^3} \int_1^\infty f_\pm(E, T, \mu) E \sqrt{E^2 - 1} dE, \quad (49)$$

where E is the relativistic particle energy in units of $m_e c^2$. Here f_\pm is the Fermi-Dirac function,

$$f_\pm(E, T, \mu) = \frac{1}{\exp[(E \pm \mu)/\Theta] + 1}, \quad (50)$$

where $\Theta = k_B T/m_e c^2$ and $\mu \equiv \mu_- = -\mu_+$ is the electron chemical potential in units of $m_e c^2$. Charge neutrality requires that

$$n_- - n_+ = Y_e n_b, \quad (51)$$

which, together with Eq. (49), determines μ and n_\pm at a given thermodynamic state (ρ, T, Y_e) . For degenerate relativistic matter ($\mu/\Theta \gg 1$), using the Sommerfeld expansion of Eq. (49) in terms of μ/Θ , one can show that the temperature dependence of μ is approximately given by (see Appendix A)

$$\sqrt{\mu^2 - 1} = \sqrt{E_F^2 - 1} \left(1 - \frac{\pi^2}{6} \frac{\Theta^2}{E_F^2 - 1} \right), \quad (52)$$

where $E_F \equiv \mu(T=0)$ is the Fermi energy. Furthermore, for degenerate matter, free e^\pm pairs can only be obtained from around the Fermi edge $E \simeq \mu$ with width $\Delta E \simeq 4\Theta$, which is very narrow ($\Delta E/E \simeq 4\Theta/\mu \ll 1$); from Eq. (49), one finds that for $\mu/\Theta \gg 1$, $E \simeq \mu$,

$$\frac{n_+}{n_-} \propto \exp(-2\mu/\Theta), \quad (53)$$

i.e., e^\pm creation is heavily suppressed. Higher electron degeneracy $\eta \equiv \mu/\Theta$ results in less electrons and positrons (cf. Eqs. (49) and (53)). This decreases the neutrino emission via charged-current interactions and pair annihilation (cf. Eqs. (27)–(30)); i.e., it results in a lower cooling rate and higher temperatures. Higher temperatures, in turn, decrease μ (cf. Eq. (52)) and thus increase the degeneracy, i.e., η . Because of this negative feedback loop, whenever the disk enters the (strongly) degenerate regime, it will tend to self-regulate its degeneracy and maintain a state of mild electron degeneracy $\eta \sim 1$. Indeed, as shown by Fig. 5, soon after reaching the quasi-stationary state, the disk has regulated itself to mild degeneracy $\eta \sim 1$ in the inner parts of the disk in which neutrino cooling is energetically important ($r \lesssim 60$ km or $r \lesssim 14$ gravitational radii) and qualitatively remains in this state throughout the remainder of the simulation.

In the hot and dense matter of the inner parts of the disk, electron and positron capture (cf. Eqs. (27) and (28)) are the dominant cooling reactions. The equilibrium Y_e that results from conditions of mild degeneracy

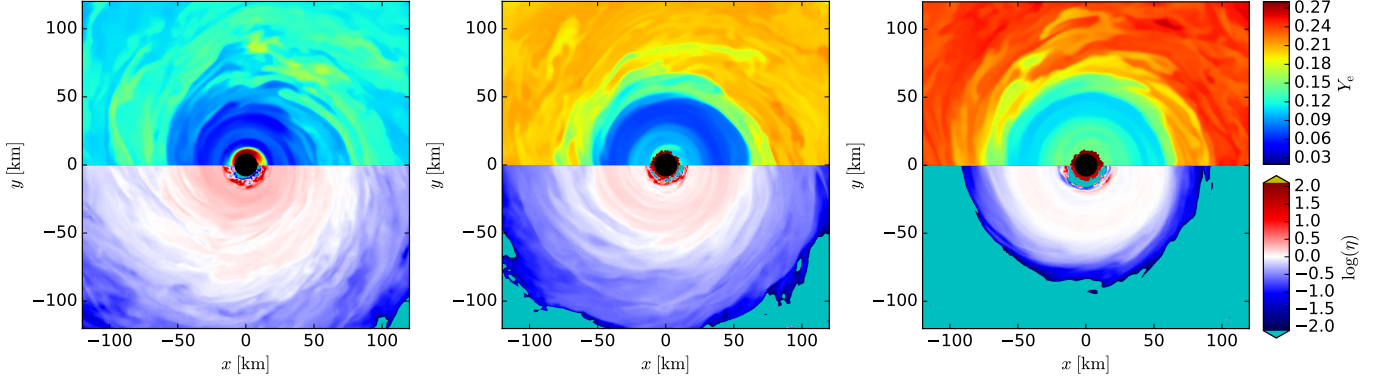


Figure 5. Electron fraction Y_e and normalized electron chemical potential $\eta = \mu/\Theta$ at $t = 43$ ms (left), $t = 130$ ms (center), and $t = 250$ ms (right), showing a mildly degenerate state and low Y_e in the inner parts of the disk as a result of self-regulation (Sec. 4.3).

in this neutrino-transparent matter is then determined by equal rates of e^\pm capture,

$$\dot{n}_{e-p} = \dot{n}_{e+n}; \quad (54)$$

i.e., Eqs. (49), (51), and (54) determine Y_e for a given ρ and T . For mild degeneracy $\eta \gtrsim 1$, one can show that from Eq. (54), the equilibrium Y_e is approximately given by (Beloborodov 2003)

$$Y_e = 0.5 + \frac{7\pi^4}{1350\zeta(5)} \left(\frac{Q}{2\Theta} - \eta \right) \quad (55)$$

$$= 0.5 + 0.487 \left(\frac{1.2655}{\Theta} - \eta \right), \quad (56)$$

where ζ is the Riemann ζ -function and $Q = (m_n - m_p)/m_e = 2.531$ is the neutron–proton mass difference in units of the electron mass. A very mild electron degeneracy $\eta \gtrsim 1$ in hot matter $\Theta \approx 1$ is therefore sufficient to generate conditions of neutron richness $Y_e < 0.5$. For the hot $\Theta \gtrsim 1$ and mildly degenerate conditions $\eta \gtrsim 1$ of the inner parts of the disk, the resulting neutron richness adjusts to an equilibrium value of typically $Y_e \sim 0.1$ or lower (see Fig. 5).

The presence of this self-regulation mechanism to mild electron degeneracy, which implies a low $Y_e \sim 0.1$, is important to allow for the generation of neutron-rich outflows that can undergo r -process nucleosynthesis (Secs. 4.4 and 5). It forces the disk to keep a reservoir of neutron-rich material despite the ongoing protonization process in the rest of the disk—neutron-rich material that is continuously fed into the outflows to keep the overall mean electron fraction \bar{Y}_e of the outflow rather low over the lifetime of the disk ($\bar{Y}_e \sim 0.2$, see Tab. II of Siegel & Metzger 2017 and Sec. 5.2). This results in the possibility of generating a robust second-to-third-peak r -process (cf. Sec. 5) and thus the production of a significant amount of lanthanide material in the outflow. Due to its high opacity, this material can then produce a red KN, as observed in the recent GW170817 event.

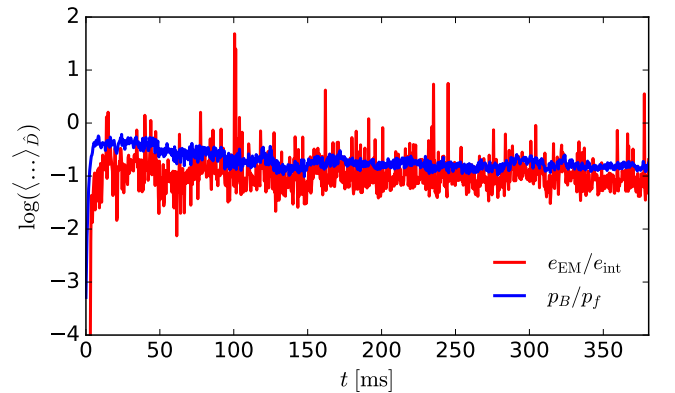


Figure 6. Evolution of the density-averaged ratio of the electromagnetic to internal energy (red) and of the magnetic-to-fluid pressure ratio (blue), indicating a steady turbulent state of the disk.

4.4. Magnetic dynamo, disk corona, and generation of outflows

Magnetic stresses generated by MHD turbulence via the MRI mediate angular momentum transport and thus energy dissipation in the disk. Turbulence also dissipates magnetic energy, which, however, is regenerated through a dynamo (e.g., Parker 1955; Brandenburg et al. 1995). The balance of the two processes results in a saturated steady turbulent, quasi-equilibrium state, which is characterized by a roughly constant ratio of magnetic to internal energy in the disk.

Figure 6 shows the temporal evolution of the density-averaged ratio of electromagnetic to internal energy $\langle e_{\text{EM}}/e_{\text{int}} \rangle_{\hat{D}}$ and of the magnetic-to-fluid pressure ratio $\langle p_B/p_f \rangle_{\hat{D}}$, which are indeed indicative of a disk in a steady turbulent state. We define the rest-mass density average of a quantity χ by

$$\langle \chi \rangle_{\hat{D}} \equiv \frac{\int \chi \hat{D} d^3x}{\int \hat{D} d^3x}, \quad (57)$$

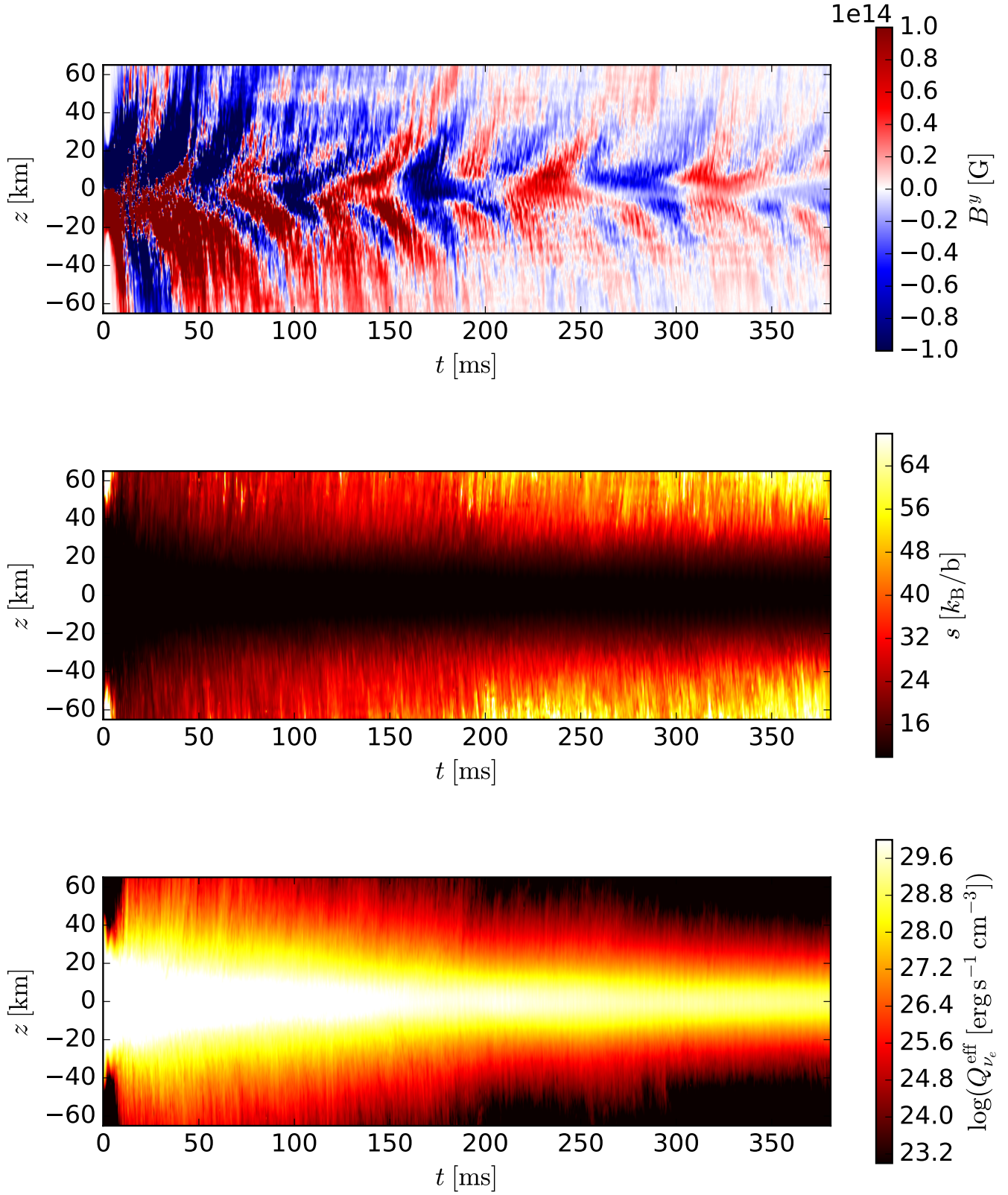


Figure 7. Spacetime diagrams of the y -component of the magnetic field (top), the specific entropy (center), and the effective electron neutrino energy emission rate per volume (bottom; representative of neutrino cooling), radially averaged between 30 and 70 km from the rotation axis in the x - z (meridional) plane as a function of height z relative to the equatorial plane.

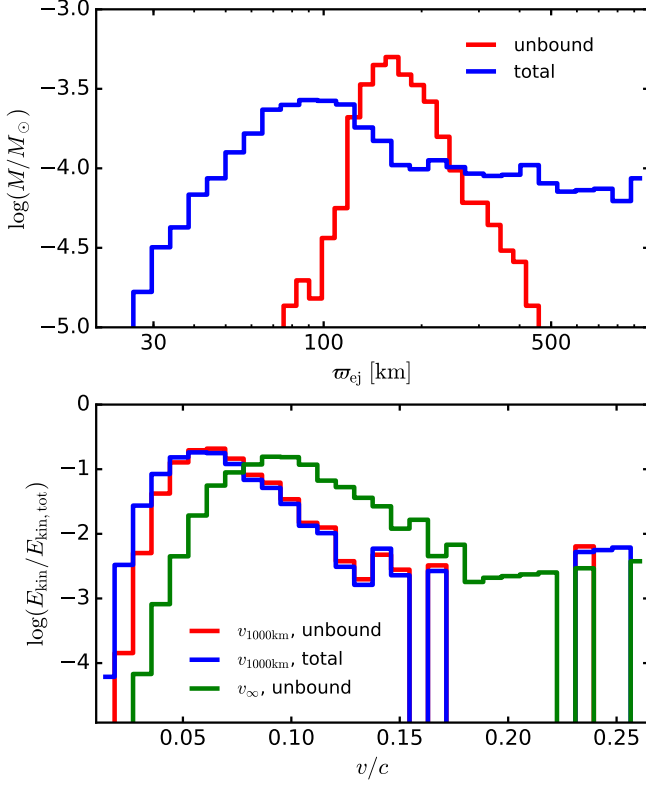


Figure 8. Top: mass distributions of the unbound and total disk outflow as measured by tracer particles in terms of their cylindrical radius ϖ_{ej} at the time of ejection from the disk (corona). Bottom: distribution of kinetic energy (in units of the respective total kinetic energy) of the unbound and total disk outflow in terms of the outflow velocity $v_{1000\text{km}}$ measured at $r = 10^3$ km from the BH and of the unbound outflow in terms of the corresponding asymptotic escape velocity v_∞ (see text).

where $\hat{D} = \sqrt{\gamma}\rho W$ is the conserved rest-mass density (cf. Eqs. (7)–(9)).⁸ Following Duez et al. (2006), we define the total internal energy

$$E_{\text{int}} \equiv \int \epsilon \rho W \sqrt{\gamma} d^3x \quad (58)$$

and the total electromagnetic energy

$$E_{\text{EM}} \equiv \int n_\mu n_\nu T_{\text{EM}}^{\mu\nu} \sqrt{\gamma} d^3x, \quad (59)$$

where $T_{\text{EM}}^{\mu\nu}$ is the electromagnetic part of the energy–momentum tensor. We thus define the local ratio of electromagnetic to internal energy by

$$\frac{e_{\text{EM}}}{e_{\text{int}}} \equiv \frac{n_\mu n_\nu T_{\text{EM}}^{\mu\nu}}{\epsilon \rho W}. \quad (60)$$

⁸ Here and in the following, spatial integrals refer to the entire simulation domain, excluding the interior of the BH horizon.

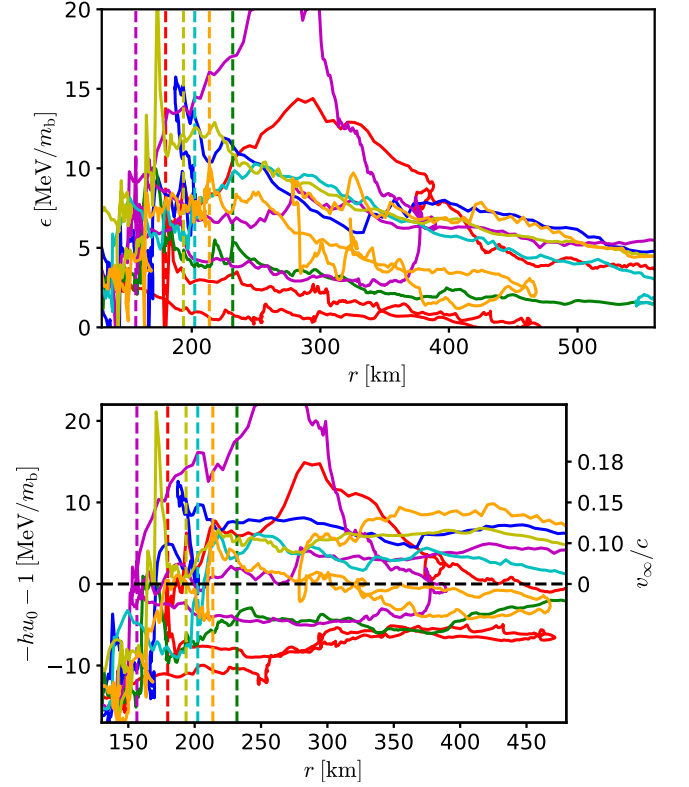


Figure 9. Representative tracer particles: specific internal energy (top) and Bernoulli criterion for unboundedness and corresponding asymptotic escape velocity (bottom) as a function of radial coordinate distance from the BH. Vertical dashed lines mark the corresponding radii at which 50% of the total α -particle production along the trajectory has been accomplished, i.e., the last time where the α -particle mass fraction $X_\alpha = 0.5X_{\alpha,\text{max}}$, where $X_{\alpha,\text{max}} = 2Y_{e,\text{max}}$, with $Y_{e,\text{max}}$ being the maximum electron fraction along the particle trajectory.

Figure 6 shows that for $t > 20$ ms, this ratio remains roughly constant in a time-averaged sense and thus indicates that a steady turbulent state of the disk is indeed achieved and maintained. Furthermore, Fig. 6 shows that

$$\left\langle \frac{p_B}{p_f} \right\rangle_{\hat{D}} \simeq 0.1, \quad (61)$$

which is also characteristic of such a steady turbulent state (e.g., Jiang et al. 2014b; Sądowski et al. 2015). This ratio in the nonlinear saturated state is much larger than the initial value of $p_B/p_f < 5 \times 10^{-3}$ (cf. Sec. 3 and Tab. 1).

The 3D nature of our disk simulation is crucial for generating a steady turbulent state. Due to the antidy-namo theorem (Cowling 1933), magnetic fields cannot be regenerated by dynamo action in axisymmetry, and a steady turbulent state cannot thus be maintained.

Direct evidence for dynamo action in our disk simulation is depicted in the top panel of Fig. 7, which shows a

spacetime diagram of the radially averaged y -component of the magnetic field in the x - z plane. This “butterfly” diagram clearly indicates the presence of magnetic cycles with a period of roughly ~ 20 ms throughout the entire simulation time domain. In the disk midplane, magnetic fields of temporally alternating polarity are generated by MHD turbulence. These fields slowly migrate off the midplane by magnetic pressure gradients and buoyancy, where they are gradually dissipated into heat. This migration and dissipation of magnetic energy contributes to establishing a “hot” corona above and below the midplane, as indicated by the middle panel of Fig. 7. This spacetime diagram of the specific entropy shows strongly increasing specific entropies off the midplane where magnetic field strengths decrease. We note that the temperature, however, decreases as a function of height off the midplane. Therefore, the production of high-energy nonthermal neutrinos in the corona by up-scattering of thermal neutrinos emitted from the midplane (cf. bottom panel of Fig. 7) is not expected.⁹

In the hot corona, powerful outflows are generated. In these regions of lower density, viscous heating from MHD turbulence and dissipation of magnetic energy exceeds cooling by neutrino emission, which is strongest in the disk midplane (cf. Fig. 7, bottom panel). This heating-cooling imbalance results in launching neutron-rich winds from the disk. Above and below the midplane, the neutrino emissivities decrease as functions of “height” $|z|$, and the weak interactions (and thus Y_e) essentially “freeze out”; however, further mixing in the (initially turbulent) outflows can still change Y_e .

The outflows are tracked by 10^4 passive tracer particles that are advected with the plasma. These tracer particles are of equal mass, placed within the initial torus at $t = 0$ ms with a probability proportional to the conserved rest-mass density $\hat{D} = \sqrt{\gamma}\rho W$. We distinguish between total outflow, defined as the entity of all tracer particles that have reached a radial coordinate distance of 10^3 km from the center of the BH by the end of the simulation, and unbound outflow, or ejecta, defined as the entity of tracer particles that are additionally unbound according to the Bernoulli criterion $-hu_0 > 1$ (nonvanishing escape velocity at infinity).

Outflows are generated over a wide range of radii. This is illustrated by the top panel of Fig. 8, which shows mass histograms of the outflow tracer particles in terms of their cylindrical coordinate radii $\varpi = \sqrt{x^2 + y^2}$ at the time of ejection from the disk, $\varpi_{\text{ej}} \equiv \varpi(t = t_{\text{ej}})$. We define the time of ejection from the disk or corona $t = t_{\text{ej}}$ as the time after which the radial coordinate position of a

tracer particle $r = \sqrt{x^2 + y^2 + z^2}$ only increases monotonically with time. The total outflow shows a broad distribution with significant mass being ejected between $\varpi_{\text{ej}} \approx 20$ km and $\varpi_{\text{ej}} > 600$ km from the BH. However, we find that mass ejection is most efficient in a narrower range of ejection radii, as indicated by the histogram of unbound matter, the latter being ejected essentially in the range $\varpi_{\text{ej}} \approx 100 - 400$ km from the BH.

Matter is typically unbound by recombination into α -particles. The imbalance of heating and cooling in the hot corona, as mentioned above, lifts material in the BH potential but typically only leads to marginally bound or marginally unbound outflows. Subsequent nuclear binding energy release from recombination of free nucleons into α -particles rapidly generates specific enthalpy as matter approaches the recombination temperature and immediately “unbinds” the material; this is shown in Fig. 9 for a few representative tracer particles. A spike in the specific enthalpy h is created by internal energy that becomes available during the recombination process (7 MeV per baryon per α -particle produced) plus the resulting pressure increase in a low-density environment. For a stationary relativistic fluid flow (isentropic, constant specific angular momentum), hu_0 is constant along a fluid world line (Eq. (44)). As the material moves away from the disk, the outflows cool ($h \rightarrow 1$) and specific enthalpy is converted into kinetic energy keeping hu_0 constant, which sets the asymptotic escape velocity.

The bottom panel of Fig. 8 shows the distribution of kinetic energy of the unbound and total outflows in terms of their outflow velocities. We characterize the outflow by two velocities: $v_{1000\text{km}}$, the velocity at a coordinate distance $r = 10^3$ km from the BH, and v_∞ , the corresponding asymptotic escape velocity when the conversion of internal energy to kinetic energy has been completed. Here v_∞ is computed from the corresponding asymptotic Lorentz factor $W_\infty \equiv -hu_0$, where hu_0 is evaluated either when the tracer particle leaves the computational domain or at the final time of the simulation if it stays inside the computational domain for the entire simulation time. Unbound and total outflows have similar velocity distributions in the range $v_{1000\text{km}} \approx (0.03 - 0.15)c$. The kinetic energy-weighted mean outflow velocities $\bar{v}_{1000\text{km}} \equiv \sqrt{2E_{\text{kin,tot}}/M_{\text{ej}}}$ are $0.063c$ and 0.058 for unbound and total outflow, respectively. Here $E_{\text{kin,tot}}$ denotes the total kinetic energy in the outflow type, and M_{ej} is the total mass of the outflow type. The asymptotic kinetic energy distribution of the unbound outflow, however, shows $v_\infty \approx (0.04 - 0.25)c$, with a higher kinetic energy-weighted mean of $\bar{v}_\infty = 0.094c \approx 0.1c$.

Though not included in our simulations, the outflows will receive additional nuclear heating from the r -process on larger radial scales of $\approx 2 - 3$ MeV per nucleon (Metzger et al. 2010a), which will boost its speed by an additional $\approx 10 - 20\%$. We note that \bar{v}_∞ of the unbound

⁹ Furthermore, the production of high-energy nonthermal neutrinos by electron-positron pair annihilation in the corona is also not expected, as thermalization processes (e.g., Coulomb scattering) are extremely rapid, which would suppress any nonthermal electron tail above the mean temperature.

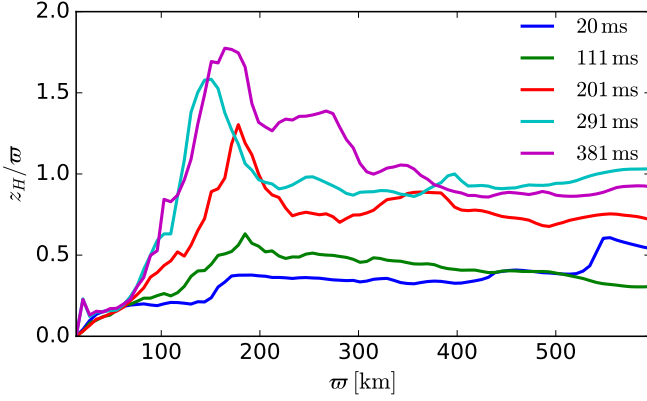


Figure 10. Density scale height of the disk at different times during the evolution.

outflow corresponds to the kinetic energy-averaged value $v_{\text{KN}} \approx 0.1c$, similar to that required to explain the red KN component observed in the recent GW170817 event (e.g. Chornock et al. 2017; Villar et al. 2017).

The total unbound mass from the disk at the end of the simulation amounts to $\approx 20\%$ of its initial value. However, the true total ejecta mass, including late times after the simulation has terminated, is likely to be roughly twice as great, as estimated in greater detail in the following subsection. Additional properties of the outflow are summarized in Siegel & Metzger (2017).

4.5. Global disk structure and long-term evolution

The global disk structure as characterized by the radial profile of the vertical density scale height is shown in Fig. 10. We define the scale height according to

$$z_H(\varpi) \equiv \langle |z| \rangle_{\hat{D}, \text{cyl}}, \quad (62)$$

where

$$\langle \chi \rangle_{\hat{D}, \text{cyl}} \equiv \frac{\int \int_0^{2\pi} \chi \hat{D} \varpi d\phi dz}{\int \int_0^{2\pi} \hat{D} \varpi d\phi dz} \quad (63)$$

is the rest-mass density average of a quantity χ over azimuthal angle ϕ and height z as a function of the cylindrical coordinate radius ϖ .

At large radii, $\varpi \gtrsim 250$ km, the disk remains geometrically thick at all times, with a density scale height of $z_H/\varpi \gtrsim 0.4-1$. This is because neutrino cooling is always inefficient in these low-density regions, as illustrated by the radial profile of the density-averaged electron neutrino emission rate $\langle Q_{\nu_e}^{\text{eff}} \rangle_{\hat{D}, \text{cyl}}$ in Fig. 11. At late times, $t > 200$ ms, the density scale height z_H/ϖ exceeds unity in the radial region $\varpi \approx 100-300$ km, which is due to the outflows being efficiently generated at these radii (see Sec. 4.4, Fig. 8). The thickening of the disk as the accretion drops and the concomitant generation of outflows was predicted by 1D (height-integrated) models (Metzger et al. 2008a, 2009).

The disk becomes thinner at smaller radii, starting at the characteristic radius ϖ_α , where α -particles disso-

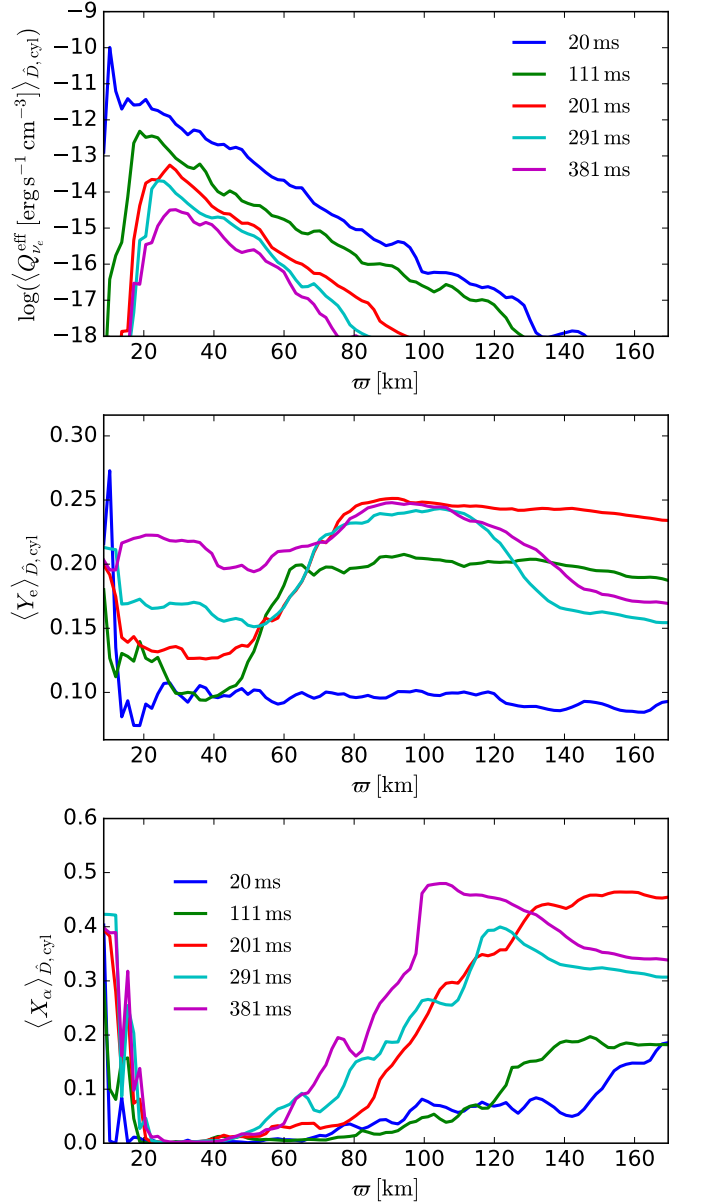


Figure 11. Density-averaged radial profiles of (top to bottom) the electron neutrino emissivity, electron fraction, and α -particle mass fraction at different times during the evolution.

ciate into free nucleons. The α -dissociation consumes 7 MeV per nucleon, which acts to cool the accretion flow and results in a geometrically thinner disk. This radius is initially at $\varpi_\alpha \approx 170$ km and decreases to $\varpi_\alpha \approx 100$ km by the end of the simulation, as indicated by the radial profile of the density-averaged α -particle mass fraction $\langle X_\alpha \rangle_{\hat{D}, \text{cyl}}$ (cf. Fig. 10 and the bottom panel of Fig. 11).

At yet smaller radii, the accretion flow becomes geometrically even thinner as the result of neutrino cooling, with the density scale height $z_H/\varpi \sim 0.1$ close to the

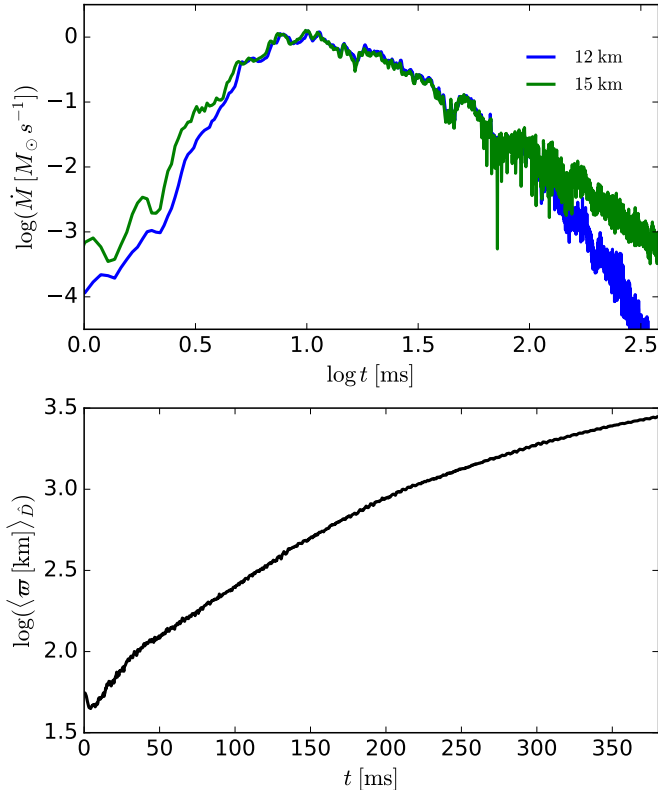


Figure 12. Top: accretion rate onto the BH as measured by the mass flux through spherical coordinate surfaces with radii 12 and 15 km. Bottom: evolution of the density-averaged cylindrical radius ϖ of the baryonic matter (cf. Eq. (57)), indicating viscous spreading of the disk.

BH, $\varpi \lesssim 70$ km (cf. Fig. 10). This efficient neutrino cooling begins interior to the so-called “ignition” radius $\varpi_{\text{ign}} < \varpi_{\alpha}$, which is defined as the location where the neutrino-cooling timescale becomes less than the local accretion timescale (Chen & Beloborodov 2007). This radius typically coincides with the location at which the energies of electrons and positrons become comparable to the neutron–proton mass difference $(m_n - m_p)c^2$, triggering the onset of the efficient Urca cooling reactions (Eqs. (27) and (28); see Fig. 11, top panel). The same weak interactions typically result in further reduction in the electron fraction Y_e , due to the increased degeneracy of the matter, as discussed in the previous subsection (cf. Fig. 11, middle panel).

By the end of the simulation, the BH has accreted $\approx 60\%$ of the initial torus mass. The BH accretion rate as measured by the mass flux through spherical coordinate detector surfaces is shown in Fig. 12 (top panel). It decreases from $\sim 1 M_{\odot} s^{-1}$ at early times to $\sim 10^{-4} M_{\odot} s^{-1}$ by the end of the simulation. This leads to an essentially converged total accreted mass onto the BH of $\approx 1.20 \times 10^{-2} M_{\odot}$ or $\approx 0.59 M_{t,\text{in}}$. Here $M_{t,\text{in}} = 2.02 \times 10^{-2} M_{\odot}$ is the initial disk mass at

$t = 20$ ms, excluding all matter that is accreted onto the BH or ejected from the disk during the initial relaxation phase (cf. Sec. 4.1). As the accretion rate continues to decrease as the disk viscously spreads outward (see below), the total accreted disk mass is unlikely to increase by a significant amount during the subsequent evolution.

The MHD turbulence mediates angular momentum transport in the disk, which leads to accretion onto the BH but also to viscous radial spreading of the disk. Evidence for the latter effect is reported in the bottom panel of Fig. 12, which shows that the density-averaged cylindrical radius $\langle \varpi \rangle_D$ of matter in the simulation domain is monotonically growing after the initial relaxation phase. The same result is obtained when the disk corona and winds are explicitly excluded from the integration, i.e., by only integrating up to the local density scale height z_H of the disk (Eq. (62)). However, equatorial winds are not straightforward to distinguish from the disk itself and thus remain in the analysis either way.

About $\approx 40\%$ of the initial disk mass is unbound in outflows, which undergo r -process nucleosynthesis (Sec. 5). By the end of the simulation, roughly $\approx 20\%$ of the initial disk mass has already been ejected from the disk; i.e., it has reached > 1000 km and is unbound (cf. Sec. 4.4 and Tab. II of Siegel & Metzger 2017). However, the disk is still producing steady winds by the end of the simulation, which means the total unbound mass is likely to become significantly higher. Even as the disk dilutes with time and neutrino cooling becomes less important, viscous heating will still continue to drive winds. Furthermore, as the disk viscously spreads, additional material is lifted out of the BH potential, also aided by nuclear binding energy release from the formation of α -particles and heavier nuclei as the material cools. With the total accreted mass having already converged, it is thus reasonable to assume that the remaining disk mass by the end of the simulation will eventually be evaporated, leading to an estimated total ejected mass of $\lesssim 0.4 M_{t,\text{in}}$.

4.6. Neutrino emission

The inner parts of the disk are sufficiently hot and dense that neutrino emission becomes energetically important (cf. Fig. 11 and Sec. 4.5). In this section, we discuss the characteristics of the neutrino radiation from the disk, which will serve as input to our r -process nucleosynthesis calculations presented in the next section.

We define the total neutrino luminosity for each neutrino species $\nu_i \in \{\nu_e, \bar{\nu}_e, \nu_x\}$ according to (cf. Eqs. (19) and (21))

$$L_{\nu_i} = \int \alpha W Q_{\nu_i}^{\text{eff}} \alpha \sqrt{\gamma} d^3x, \quad (64)$$

where an additional factor α is included to correct for the gravitational redshift due to the BH potential. This definition takes into account the effects of finite optical depth; i.e., it is based on the effective energy emission

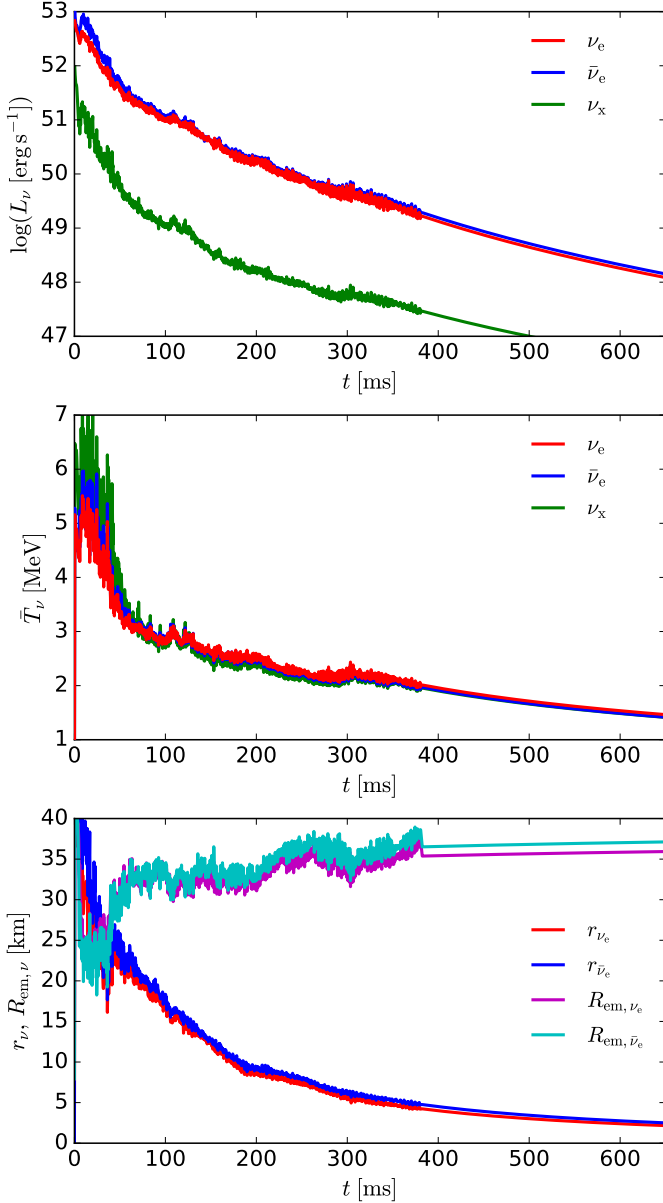


Figure 13. Characteristics of neutrino emission from the disk (top to bottom): total neutrino luminosity, mean neutrino temperature, and characteristic radii of neutrino emission (see the text). After the end of the simulation ($t = 381$ ms), quantities are extrapolated by power laws fit to the late-time simulation data.

rates, but it neglects reabsorption of emitted neutrinos by matter.

Neutrino emission is purely thermal, characterized by the local emission temperature T (the temperature of matter). We assign mean neutrino emission temperatures for the different neutrino species to the disk, defined as the neutrino energy emission rate averaged quantities

$$\bar{T}_{\nu_i} \equiv \langle T \rangle_{Q_{\nu_i}}. \quad (65)$$

Here we have defined the neutrino emission rate average of a quantity χ by

$$\langle \chi \rangle_{Q_{\nu_i}} \equiv \frac{\int \chi Q_{\nu_i}^{\text{eff}} W \alpha \sqrt{\gamma} d^3x}{\int Q_{\nu_i}^{\text{eff}} W \alpha \sqrt{\gamma} d^3x}. \quad (66)$$

Note that $Q_{\nu_i}^{\text{eff}} W \alpha \sqrt{\gamma}$ corresponds to the energy emitted per unit time and coordinate volume through neutrinos of species ν_i as seen by the Eulerian observer (cf. Eqs. (19) and (21)). For further reference, we also define a corresponding spherical blackbody emission radius,

$$r_{\nu_i} = \left(\frac{L_{\nu_i}}{4\pi \frac{7}{16} \sigma \bar{T}_{\nu_i}^4} \right)^{\frac{1}{2}}, \quad (67)$$

where σ is the Stefan–Boltzmann constant and the actual characteristic neutrino emission radius

$$R_{\text{em},\nu_i} \equiv \langle r \rangle_{Q_{\nu_i}}. \quad (68)$$

Figure 13 shows the total neutrino luminosities, average neutrino emission temperatures, and blackbody as well as characteristic emission radii as extracted from our simulation data. We extrapolate quantities beyond the end of the simulation at $t = 381$ ms by power laws fitted to the late-time simulation data.

The neutrino luminosities are initially high, with $L_{\nu} \sim 10^{52}$ erg s $^{-1}$ for electron and anti-electron neutrinos and at least an order of magnitude lower for the heavier neutrino species, but they quickly fade over timescales of hundreds of ms. We note that these initial neutrino luminosities are very similar to the values found in the early post-merger accretion systems of recent hydrodynamic NS–NS and BH–NS merger simulations (e.g., Sekiguchi et al. 2016; Radice et al. 2016; Foucart et al. 2017). The total energy radiated in neutrinos by the disk in terms of the various neutrino species is given by $E_{\nu_e}, E_{\bar{\nu}_e}, E_{\nu_x} = (4.2, 6.1, 0.083) \times 10^{50}$ erg. Despite the fact that the neutrino luminosities fade rapidly compared to the evolution timescale of the disk, irradiation by neutrinos during the early phase of the evolution can still have an appreciable effect on the composition of the disk outflows and thus on r -process nucleosynthesis. We discuss this effect in the following section.

5. R -PROCESS NUCLEOSYNTHESIS

Abundance yields from r -process nucleosynthesis in the outflows of the accretion disk were already presented in Siegel & Metzger (2017). Here we elaborate on these results, discuss the nucleosynthesis anomaly at $A = 132$ (Sec. 5.1), and present results from r -process nucleosynthesis calculations including neutrino absorption, which we perform with the nuclear-reaction network SkyNet (Lippuner & Roberts 2017; Sec. 5.2).

5.1. The $A=132$ anomaly

Previous r -process nucleosynthesis analyses of disk outflows from 2D Newtonian α -disk simulations have

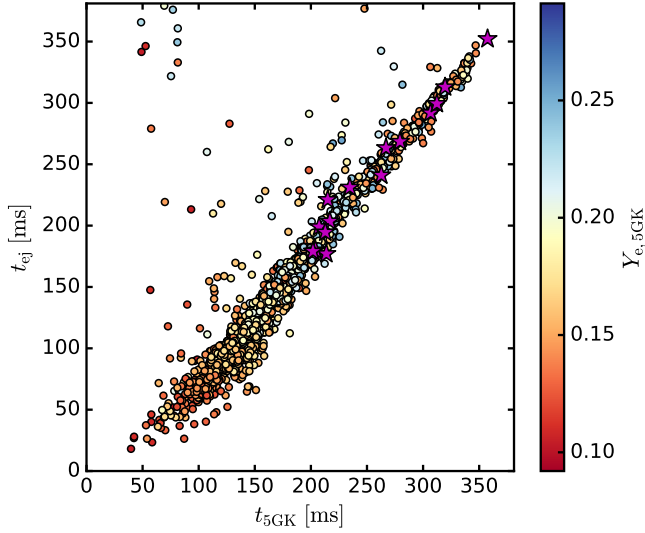


Figure 14. Ejection time t_{ej} of all unbound tracer particles versus the last time t_{5GK} at which the tracer particle reached a temperature of 5 GK, color-coded by the electron fraction at t_{5GK} . The 15 tracer particles that contribute most to the nucleosynthesis anomaly at $A = 132$ are marked as magenta stars, which all follow the main correlation between t_{ej} and t_{5GK} .

noted an overproduction of $A = 132$ nuclei with respect to the second r -process peak ($A = 128 - 130$) when compared to observed solar system abundances (Wu et al. 2016). This was ascribed to late-time, low-temperature convection in the disk outflow, i.e., to fluid elements, whose ejection time t_{ej} (cf. Sec. 4.4) from the disk is much greater than t_{5GK} . We define t_{5GK} as the last time when the temperature of a fluid element (tracer particle) decreased below 5 GK, which is the characteristic temperature for NSE to break down and the r -process to set in.

Although our 3D GRMHD setup is expected to show less large-scale, low-temperature convection than 2D viscous hydrodynamics (because of the inverse turbulent cascade in 2D), we still find an overproduction at $A = 132$, which is evident from Fig. 15.

In contrast to Wu et al. (2016), we find that this anomaly in our 3D GRMHD setup is not predominantly due to tracers that undergo late-time low-temperature convection, i.e., for which $t_{ej} \gg t_{5GK}$. This is shown in Fig. 14, which reports t_{ej} vs. t_{5GK} for all unbound tracer particles. The dominant contributors to this anomaly all follow the main correlation between t_{ej} and t_{5GK} , and tracers with $t_{ej} \gg t_{5GK}$ are not among those. The origin of this anomaly remains inconclusive at this point. It may point to a nuclear origin at least for our present calculations with SkyNet, which requires further investigation concerning the nuclear physics input.

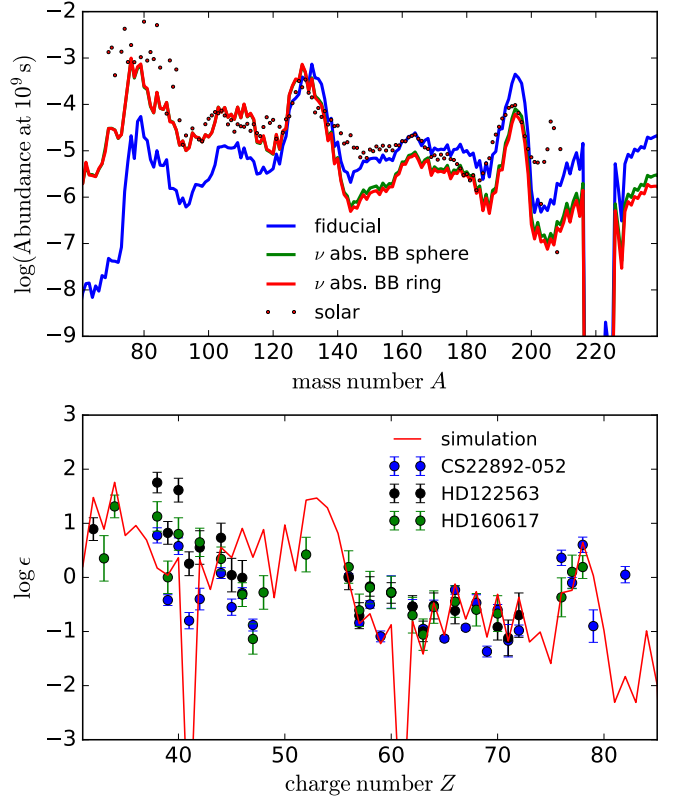


Figure 15. Top: final mean elemental abundances for the fiducial case without neutrino absorption as in Siegel & Metzger (2017) and including neutrino absorption according to a spherical blackbody light-bulb scheme (see the text; “ ν abs. BB sphere”) and according to ringlike blackbody emission (see the text; “ ν abs. BB ring”). For reference, observed solar system abundances from Arnould et al. (2007) are added, scaled to match the fiducial mean abundances at $A = 130$. Bottom: comparison of abundances including neutrino absorption according to the ringlike blackbody emission to the observed abundances in metal-poor halo stars (Snedden et al. 2003; Roederer & Lawler 2012; Roederer et al. 2012), showing $\log \epsilon = \log Y_Z/Y_1 + 12$, scaled such that $\sum (\log Y_Z/Y_{Z,CS22892-052})^2$ is minimized in the range $55 \leq Z \leq 75$.

5.2. r -process nucleosynthesis including neutrino absorption

In order to explore the effects of neutrino absorption on r -process nucleosynthesis in the ejecta material, we ‘light-bulb’ irradiate the ejecta by neutrinos from the disk in a postprocessing step, employing two different assumptions to bracket the uncertainties in the neutrino emission geometry.

Spherical blackbody. In a first approach, following Roberts et al. (2017), we assume that neutrinos are emitted with luminosity L_{ν_i} and temperature \bar{T}_{ν_i} from a single spherical surface centered on the BH of radius r_{ν_i} (cf. Eqs. (64), (65), and (67)) and that they follow a

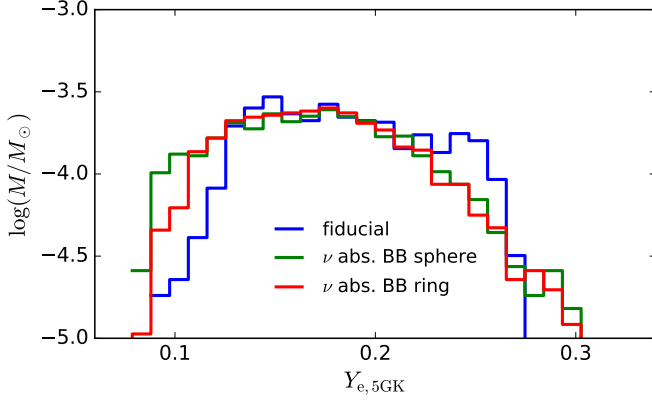


Figure 16. Comparison of the mass distributions of unbound tracer particles in terms of their electron fraction at $t = t_{5\text{GK}}$ for the fiducial case without neutrino absorption, as in Siegel & Metzger (2017), and including neutrino absorption according to a spherical blackbody light-bulb scheme (see the text; “ ν abs. BB sphere”) and according to ringlike blackbody emission (see the text; “ ν abs. BB ring”).

Fermi-Dirac distribution in energy space,

$$f_{\text{FD}}(E, \bar{T}_{\nu_i}) = \frac{1}{\exp(E/k_{\text{B}}\bar{T}_{\nu_i}) + 1}, \quad (69)$$

where E denotes the neutrino energy. The radii of the neutrinospheres r_{ν_i} are typically on the order of tens of km and are roughly comparable to or smaller than the actual radii R_{em,ν_i} of the peak neutrino emission within the disk (see Fig. 13, bottom panel). The neutrino distribution function in energy space as a function of coordinate radius r for species ν_i is then given by

$$f_{\nu_i}(E, r; \bar{T}_{\nu_i}, L_{\nu_i}) = \frac{1}{2} \left(1 - \sqrt{1 - \frac{r_{\nu_i}^2}{r^2}} \right) f_{\text{FD}}(E, \bar{T}_{\nu_i}). \quad (70)$$

Ringlike blackbody. In a second approach, following the neutrino emission geometry of Fernández & Metzger (2013), we assume that neutrinos are emitted with luminosity L_{ν_i} and temperature \bar{T}_{ν_i} from a ring of radius R_{em,ν_i} in the equatorial plane around the BH (cf. Eqs. (64), (65), and (68)). This geometry more closely resembles neutrino emission from the disk, as most of the emission is confined to regions close to the midplane (cf. Fig. 7, bottom panel) and as the effective emission rates $Q_{\nu_i}^{\text{eff}}$ are indeed sharply peaked around some characteristic emission radius $r \simeq R_{\text{em},\nu_i}$ (cf. Fig. 11, top panel). In analogy to Eq. (70), the neutrino distribution function in this case is given by

$$f_{\nu_i}(E, r, \theta; \bar{T}_{\nu_i}, L_{\nu_i}, R_{\text{em},\nu_i}) = \frac{1}{2} N_{\nu_i} \mathcal{I}_{\nu_i} f_{\text{FD}}(E, \bar{T}_{\nu_i}), \quad (71)$$

where

$$N_{\nu_i} = \frac{L_{\nu_i}}{4\pi R_{\text{em},\nu_i}^2 \frac{7}{16} \sigma \bar{T}_{\nu_i}^4} \quad (72)$$

and

$$\mathcal{I}_{\nu_i} = \frac{1}{2\pi} \left(\frac{R_{\text{em},\nu_i}}{r} \right)^2 \int_0^{2\pi} \frac{d\phi_{\text{R}}}{2D(r, \theta, R_{\text{em},\nu_i}, \phi_{\text{R}})/r^2}. \quad (73)$$

Here r and θ denote the radial coordinate and polar angle, respectively, and ϕ_{R} denotes the azimuthal angle that parameterizes the neutrino emission ring. Furthermore,

$$D = r \left[1 + \left(\frac{R_{\text{em},\nu_i}}{r} \right)^2 - 2 \frac{R_{\text{em},\nu_i}}{r} \sin \theta \cos \phi_{\text{R}} \right]^{1/2} \quad (74)$$

is the distance between a spatial point (r, θ) and the neutrino emission ring at position ϕ_{R} (cf. Fig. B2 of Fernández & Metzger 2013).

Figure 15 reports detailed abundance yields, including neutrino absorption, computed with the two methods outlined above, in comparison to previous results obtained by neglecting neutrino absorption (Siegel & Metzger 2017). It is reassuring that these results do not depend on the method by which neutrino absorption is included; both approaches lead to essentially the same abundance yields. This is not surprising, given that the source of neutrino radiation with a diameter of essentially 60–80 km is sufficiently compact compared to the spatial size of the entire disk and outflows (cf. Sec. 4.5).

With neutrino absorption included, the production of the entire range of r -process nuclei from the first to the third peak of the r -process can be explained. Including neutrino absorption dramatically improves the agreement between the abundance yields of the lighter nuclei from the first to the second r -process peak ($A \sim 80 - 120$) compared to the observed solar system abundances. This is due to neutrinos irradiating part of the outflow and the outer parts of the disk, thereby raising Y_e in part of the outflow (see Fig. 16), which enhances the production of lighter r -process nuclei. However, a strong second-to-third-peak r -process is still maintained. The fact that the outflow well reaches the production of third-peak elements at the required level to explain solar abundances, even in the presence of strong neutrino irradiation, is at least in part due to the self-regulation mechanism discussed in Sec. 4.3, which continuously releases very neutron rich-material into the outflow. The excellent agreement with observed abundances is also reflected in the bottom panel of Fig. 15, which compares the abundance yields from our simulation including neutrino absorption with observed abundances in metal-poor stars in the halo of the Milky Way.

6. CONCLUSION

Below, we summarize our main results and conclusions.

- (i) We witness the onset of MHD turbulence, which quickly results in a steady turbulent state (Sec. 4.1)

and an effective initial disk configuration that is very similar to results from recent NS–NS or NS–BH merger simulations. The disk remains in this steady turbulent state for the rest of the simulation time (Fig. 6). The butterfly diagram (Fig. 7) indicates a fully operational magnetic dynamo with a secular cycle of roughly ~ 20 ms. The dynamo generates magnetic fields of alternating polarities in the disk midplane that slowly migrate to higher latitudes, where they gradually dissipate into heat in a “hot corona.”

- (ii) We find the emergence of a hot disk corona at higher latitudes. There, viscous heating from MHD turbulence and dissipation of magnetic fields is not balanced by neutrino cooling (which tracks density and thus rapidly falls off with latitude; Fig. 7), and powerful thermal outflows are launched. The energy released by α -particle formation also plays a crucial role in unbinding matter from the disk after it is lifted out of the BH gravitational potential by coronal heating. The asymptotic velocity scale of $v_\infty \approx 0.1c$ of the unbound outflows is largely set by the energy released from α -particle recombination (Fig. 9). Our results agree qualitatively with previous work by Barzilay & Levinson (2008), who explored models of steady-state outflows driven from the midplane of neutrino-cooled disks, including those powered by the dissipation of turbulent energy in the disk corona, finding that such outflows can preserve the neutron richness of the disk midplane (see also Metzger et al. 2008b).
- (iii) We observe a regulation of the electron fraction in the disk midplane by weak interactions. We identify a self-regulation mechanism based on electron degeneracy in the inner parts of the disk (where viscous heating is roughly balanced by neutrino cooling), which regulates the electron fraction to $Y_e \sim 0.1$ irrespective of the initial conditions (Sec. 4.3). This results in the formation of a reservoir of neutron-rich material, despite the ongoing protonization in the outer parts of the disk over viscous timescales (Fig. 5). This reservoir continuously feeds very neutron-rich material into the outflows, which thus keeps the overall mean electron fraction of the outflows comparatively low ($\bar{Y}_e \sim 0.2$) over viscous timescales and guarantees the production of third-peak r -process nuclei.
- (iv) We demonstrate that the EOS and weak interactions in the disk are not affected by magnetic field effects (Fig. 4).
- (v) We find that unbound outflows carry away $\lesssim 40\%$ of the initial disk mass with asymptotic escape velocities centered around $v_\infty \approx 0.1c$, with a roughly

spherical geometry (Secs. 4.4 and 4.5; Fig. 8). The total ejecta mass is given by

$$M_{\text{ej}} \simeq 10^{-2} \left(\frac{f_{\text{ej}}}{0.35} \right) \left(\frac{M_{\text{disk}}}{3 \times 10^{-2} M_\odot} \right) M_\odot, \quad (75)$$

where f_{ej} denotes the fraction of mass ejected from the original disk of mass M_{disk} . This is larger than that found by previous 2D Newtonian viscous-hydrodynamic simulations (Fernández et al. 2015; Just et al. 2015), which we attribute to additional nonlocal coronal heating that quickly evaporates disk material. With $M_{\text{disk}} \simeq \text{few} \times 10^{-2} M_\odot$ being a rather conservative lower limit on disk masses from NS mergers (e.g., Hotokezaka et al. 2013a; Ciolfi et al. 2017), we conclude that *post-merger disk winds likely represent the dominant mass ejection mechanism in NS–NS mergers*; in BH–NS mergers, tidal ejecta may still dominate, depending on the binary parameters due to the more extreme binary mass ratios expected in this case.

The asymptotic escape velocities and the quantity of wind ejecta, if extrapolated to a moderately higher initial torus mass $\approx 0.1 M_\odot$, provide a natural explanation for the red KN from the recent GW170817 event (e.g. Chornock et al. 2017; Cowperthwaite et al. 2017; Villar et al. 2017).

- (vi) The disk radiates thermal neutrinos at characteristic temperatures of $T \sim \text{few MeV}$ with rapidly declining luminosities starting at $L_\nu \sim 10^{52} \text{ erg s}^{-1}$ and total radiated energies of $E_{\nu_e}, E_{\bar{\nu}_e}, E_{\nu_x} = (4.2, 6.1, 0.083) \times 10^{50} \text{ erg}$ (Fig. 13).
- (vii) Outflows from the accretion disk are sufficiently neutron-rich to synthesize r -process elements extending up to the third peak, a result that we find is insensitive to our treatment of neutrino heating. Neutrino heating can have a moderate impact on r -process nucleosynthesis (Fig. 15), which is likely to be greater in the case of a more massive torus (Just et al. 2015). We find that by including neutrino absorption, the entire range of r -process nuclei from the first to the third r -process peak can be synthesized in the unbound outflows, in agreement with the findings of previous α -disk simulations (e.g. Wu et al. 2016).
- (viii) The production of first-to-third-peak r -process elements with relative abundances in good agreement with observed solar abundances and those on metal-poor stars in the halo of our galaxy, together with the inferred total ejecta masses (Eq. (75)) and the relatively high rate of NS–NS mergers inferred from the discovery of GW170817 (the LIGO Scientific Collaboration & the Virgo Collaboration 2017), arguably provide the strongest evidence yet,

backed by first-principle simulations, for NS mergers being the prime production site of r -process elements in the universe.

We thank A. Beloborodov, R. Fernández, R. Haas, W. Kastaun, J. Lippuner, G. Martínez-Pinedo, P. Moesta, C. Ott, Y. Qian, D. Radice, L. Roberts, and M.-R. Wu for valuable discussions. Resources supporting this work were provided by the NASA High-End Computing (HEC) Program through the NASA Advanced Super-

computing (NAS) Division at Ames Research Center. Support for this work was provided by the National Aeronautics and Space Administration through Einstein Postdoctoral Fellowship Award Number PF6-170159 issued by the Chandra X-ray Observatory Center, which is operated by the Smithsonian Astrophysical Observatory for and on behalf of the National Aeronautics and Space Administration under contract NAS8-03060. BDM and DMS acknowledge support from NASA ATP grant NNX16AB30G and NSF grant AST-1410950.

APPENDIX

A. TEMPERATURE DEPENDENCE OF ELECTRON CHEMICAL POTENTIAL

In this appendix, we derive the temperature dependence of the chemical potential μ of electrons in relativistic degenerate matter (Eq. (52)). We start by writing the electron number density (Eq. (49)) as

$$n_- = \frac{(m_e c)^3}{\pi^2 \hbar^3} \int_{-\infty}^{\infty} f_-(E, T, \mu) g(E) dE, \quad (\text{A1})$$

with

$$g(E) \equiv \begin{cases} E\sqrt{E^2 - 1} & , E \geq 1 \\ 0 & , E < 1. \end{cases} \quad (\text{A2})$$

Noting that (i) $g(E)$ only diverges as a power of E as $E \rightarrow \infty$, (ii) $g(E) \rightarrow 0$ as $E \rightarrow -\infty$, and (iii) $g(E)$ is well behaved at $E \sim \mu > 1$, we can make use of the Sommerfeld expansion and write

$$n_- = \frac{(m_e c)^3}{\pi^2 \hbar^3} \left\{ \int_{-\infty}^{\mu} g(E) dE + 2 \sum_{n=1}^{\infty} (1 - 2^{1-2n}) \zeta(2n) \Theta^{2n} \left[\frac{d^{2n-1} g(E)}{dE^{2n-1}} \right]_{E=\mu} \right\}, \quad (\text{A3})$$

where ζ is the Riemann ζ -function. One can easily convince oneself that, at least for the first few derivatives of $g(E)$,

$$\left[\frac{d^n g(E)}{dE^n} \right]_{E=\mu} \simeq \frac{g(\mu)}{\mu^n} \mathcal{O}(1), \quad (\text{A4})$$

where $\mathcal{O}(1)$ refers to terms of order unity. Thus, the ratio of subsequent terms in the sum of Eq. (A3) scales as η^{-2} , and for degenerate matter $\eta = \mu/\Theta \gg 1$, the sum converges rapidly. Only retaining the first two terms in Eq. (A3) results in

$$n_- \simeq \frac{(m_e c)^3}{\pi^2 \hbar^3} \left\{ \frac{1}{3} (\mu^2 - 1)^{3/2} + \frac{\pi^2}{6} \Theta^2 (\mu^2 - 1)^{1/2} \right\}. \quad (\text{A5})$$

Again to first order, this can be rewritten as

$$\left(\frac{\mu^2 - 1}{E_F^2 - 1} \right)^{1/2} \simeq \left\{ 1 - \frac{\pi^2}{6} \frac{\Theta^2}{E_F^2 - 1} \right\}, \quad (\text{A6})$$

where $E_F \equiv \mu(T = 0)$ is the relativistic Fermi energy. This is the relation to be derived.

REFERENCES

- Abbott, B. P., Abbott, R., Abbott, T. D., et al. 2017, ApJL, 848, L12
- Arcavi, I., Hosseinzadeh, G., Howell, D. A., et al. 2017, Nature, 551, 64
- Aloy, M. A., Janka, H.-T., & Müller, E. 2005, A&A, 436, 273
- Armitage, P. J. 2011, ARA&A, 49, 195

- Arnould, M., Goriely, S., & Takahashi, K. 2007, *PhR*, 450, 97
- Arnowitt, R., Deser, S., & Misner, C. W. 2008, *Gen. Rel. Grav.*, 40, 1997
- Baiotti, L., & Rezzolla, L. 2017, *Reports on Progress in Physics*, 80, 096901
- Balbus, S. A. 2003, *ARA&A*, 41, 555
- Balbus, S. A., & Hawley, J. F. 1991, *ApJ*, 376, 214
- . 1992, *ApJ*, 400, 610
- . 1998, *Reviews of Modern Physics*, 70, 1
- . 2002, *ApJ*, 573, 749
- Barnes, J., & Kasen, D. 2013, *ApJ*, 775, 18
- Barzilai, Y., & Levinson, A. 2008, *NewA*, 13, 386
- Beloborodov, A. M. 2003, *ApJ*, 588, 931
- Bernuzzi, S., Dietrich, T., Tichy, W., & Brüggmann, B. 2014, *PhRvD*, 89, 104021
- Bovard, L., Martin, D., Guercilena, F., et al. 2017, *PhRvD*, 96, 124005
- Brandenburg, A., Nordlund, A., Stein, R. F., & Torkelsson, U. 1995, *ApJ*, 446, 741
- Bruenn, S. W. 1985, *ApJS*, 58, 771
- Cerdá-Durán, P., Font, J. A., Antón, L., & Müller, E. 2008, *A&A*, 492, 937
- Chandrasekhar, S. 1960, *Proc. Natl. Acad. Sci.*, 46, 253
- Chen, W., & Beloborodov, A. M. 2007, *ApJ*, 657, 383
- Chornock, R., Berger, E., Kasen, D., et al. 2017, *ApJL*, 848, L19
- Cioffi, R., Kastaun, W., Giacomazzo, B., et al. 2017, *PhRvD*, 95, 063016
- Colella, P., & Woodward, P. R. 1984, *J. Comput. Phys.*, 54, 174. <http://www.sciencedirect.com/science/article/B6WHY-4DD1PHM-SJ/2/13d69a59afba3d6a5d6bbf1144d860aa>
- Coulter, D. A., Foley, R. J., Kilpatrick, C. D., et al. 2017, *Science*, 358, 1556
- Cowling, T. G. 1933, *MNRAS*, 94, 39. <http://dx.doi.org/10.1093/mnras/94.1.39>
- Cowperthwaite, P. S., Berger, E., Villar, V. A., et al. 2017, *ApJL*, 848, L17
- Di Matteo, T., Perna, R., & Narayan, R. 2002, *ApJ*, 579, 706
- Drout, M. R., Piro, A. L., Shappee, B. J., et al. 2017, *Science*, 358, 1570
- Duan, H., & Qian, Y.-Z. 2004, *PhRvD*, 69, 123004
- . 2005, *PhRvD*, 72, 023005
- Duez, M. D., Liu, Y. T., Shapiro, S. L., Shibata, M., & Stephens, B. C. 2006, *PhRvD*, 73, 104015
- Einfeldt, B. 1988, *SIAM J. Numer. Anal.*, 25, 294. <http://dx.doi.org/10.1137/0725021>
- Evans, P. A., Cenko, S. B., Kennea, J. A., et al. 2017, *Science*, 358, 1565
- Fernández, R., Kasen, D., Metzger, B. D., & Quataert, E. 2015, *MNRAS*, 446, 750
- Fernández, R., & Metzger, B. D. 2013, *MNRAS*, 435, 502
- . 2016, *Annual Review of Nuclear and Particle Science*, 66, 23
- Foucart, F. 2012, *PhRvD*, 86, 124007
- Foucart, F., Desai, D., Brege, W., et al. 2017, *Class. Quant. Grav.*, 34, 044002
- Freiburghaus, C., Rosswog, S., & Thielemann, F.-K. 1999, *ApJL*, 525, L121
- Friedman, J. L., & Stergioulas, N. 2013, *Rotating Relativistic Stars* (Cambridge, UK: Cambridge University Press, 2013)
- Galeazzi, F., Kastaun, W., Rezzolla, L., & Font, J. A. 2013, *PhRvD*, 88, 064009
- Goriely, S., Bauswein, A., & Janka, H.-T. 2011, *ApJ*, 738, L32
- Haensel, P., Potekhin, A. Y., & Yakovlev, D. G., eds. 2007, *Astrophysics and Space Science Library*, Vol. 326, *Neutron Stars 1: Equation of State and Structure* (New York: Springer)
- Harding, A. K., & Lai, D. 2006, *Rep. Prog. Phys.*, 69, 2631
- Harten, A. 1983, *J. Comput. Phys.*, 49, 357. <http://www.sciencedirect.com/science/article/pii/0021999183901365>
- Hawley, J. F., & Balbus, S. A. 2002, *ApJ*, 573, 738
- Hirose, S., Krolik, J. H., & Stone, J. M. 2006, *ApJ*, 640, 901
- Hotokezaka, K., Kiuchi, K., Kyutoku, K., et al. 2013a, *PhRvD*, 88, 044026
- . 2013b, *PhRvD*, 87, 024001
- Hotokezaka, K., Kyutoku, K., Okawa, H., Shibata, M., & Kiuchi, K. 2011, *PhRvD*, 83, 124008
- Jiang, Y.-F., Stone, J. M., & Davis, S. W. 2014a, *ApJ*, 784, 169
- . 2014b, *ApJ*, 796, 106
- Just, O., Bauswein, A., Pulpillo, R. A., Goriely, S., & Janka, H.-T. 2015, *MNRAS*, 448, 541
- Kasen, D., Metzger, B., Barnes, J., Quataert, E., & Ramirez-Ruiz, E. 2017, *Nature*, 551, 80
- Kasliwal, M. M., Nakar, E., Singer, L. P., et al. 2017, *Science*, 358, 1559
- Kastaun, W., Galeazzi, F., Alic, D., Rezzolla, L., & Font, J. A. 2013, *PhRvD*, 88, 021501
- Kawanaka, N., & Mineshige, S. 2007, *ApJ*, 662, 1156
- Kerr, R. P. 1963, *PhRvL*, 11, 237. <https://link.aps.org/doi/10.1103/PhysRevLett.11.237>
- Kilpatrick, C. D., Foley, R. J., Kasen, D., et al. 2017, *Science*, 358, 1583

- Kiuchi, K., Cerdá-Durán, P., Kyutoku, K., Sekiguchi, Y., & Shibata, M. 2015a, *PhRvD*, 92, 124034
- Kiuchi, K., Kyutoku, K., Sekiguchi, Y., & Shibata, M. 2017, *ArXiv e-prints*, arXiv:1710.01311
- Kiuchi, K., Sekiguchi, Y., Kyutoku, K., et al. 2015b, *PhRvD*, 92, 064034
- Kiuchi, K., Sekiguchi, Y., Shibata, M., & Taniguchi, K. 2009, *PhRvD*, 80, 064037
- Kohri, K., & Mineshige, S. 2002, *ApJ*, 577, 311
- Kohri, K., Narayan, R., & Piran, T. 2005, *ApJ*, 629, 341
- Lai, D., & Qian, Y.-Z. 1998, *ApJ*, 505, 844
- Lattimer, J. M., & Schramm, D. N. 1974, *ApJL*, 192, L145
- Lee, W. H., & Ramirez-Ruiz, E. 2007, *New Journal of Physics*, 9, 17
- Lehner, L., & Pretorius, F. 2014, *ARA&A*, 52, 661
- Li, L.-X., & Paczyński, B. 1998, *ApJL*, 507, L59
- Lichnerowicz, A. 1944, *J. Math. Pures et Appl.*, 23, 37
- Lippuner, J., & Roberts, L. F. 2015, *ApJ*, 815, 82
- . 2017, *ApJS*, 233, 18
- Lipunov, V. M., Gorbovskoy, E., Kornilov, V. G., et al. 2017, *ApJL*, 850, L1
- Löffler, F., Faber, J., Bentivegna, E., et al. 2012, *Class. Quant. Grav.*, 29, 115001
- MacFadyen, A. I., Woosley, S. E., & Heger, A. 2001, *ApJ*, 550, 410
- McCully, C., Hiramatsu, D., Howell, D. A., et al. 2017, *ApJL*, 848, L32
- Metzger, B. D. 2017, *Living Reviews in Relativity*, 20, 3
- Metzger, B. D., Arcones, A., Quataert, E., & Martínez-Pinedo, G. 2010a, *MNRAS*, 402, 2771
- Metzger, B. D., & Fernández, R. 2014, *MNRAS*, 441, 3444
- Metzger, B. D., Piro, A. L., & Quataert, E. 2008a, *MNRAS*, 390, 781
- . 2009, *MNRAS*, 396, 304
- Metzger, B. D., Thompson, T. A., & Quataert, E. 2008b, *ApJ*, 676, 1130
- Metzger, B. D., Martínez-Pinedo, G., Darbha, S., et al. 2010b, *MNRAS*, 406, 2650
- Mösta, P., Mundim, B. C., Faber, J. A., et al. 2014, *Class. Quant. Grav.*, 31, 015005
- Narayan, R., Paczynski, B., & Piran, T. 1992, *ApJ*, 395, L83
- Narayan, R., Piran, T., & Kumar, P. 2001, *ApJ*, 557, 949
- Neilsen, D., Liebling, S. L., Anderson, M., et al. 2014, *PhRvD*, 89, 104029
- Nicholl, M., Berger, E., Kasen, D., et al. 2017, *ApJL*, 848, L18
- Nouri, F. H., Duez, M. D., Foucart, F., et al. 2017, *ArXiv e-prints*, arXiv:1710.07423
- O'Connor, E., & Ott, C. D. 2010, *Class. Quant. Grav.*, 27, 114103
- Oechslin, R., & Janka, H.-T. 2006, *MNRAS*, 368, 1489
- Ott, C. D., Abdikamalov, E., Mösta, P., et al. 2013, *ApJ*, 768, 115
- Parker, E. N. 1955, *ApJ*, 122, 293
- Perego, A., Cabezón, R. M., & Käppeli, R. 2016, *ApJS*, 223, 22
- Perego, A., Rosswog, S., Cabezón, R. M., et al. 2014, *MNRAS*, 443, 3134
- Popham, R., Woosley, S. E., & Fryer, C. 1999, *ApJ*, 518, 356
- Radice, D., Galeazzi, F., Lippuner, J., et al. 2016, *MNRAS*, 460, 3255
- Rezzolla, L., Baiotti, L., Giacomazzo, B., Link, D., & Font, J. A. 2010, *Class. Quant. Grav.*, 27, 114105
- Roberts, L. F., Lippuner, J., Duez, M. D., et al. 2017, *MNRAS*, 464, 3907
- Roederer, I. U., & Lawler, J. E. 2012, *ApJ*, 750, 76
- Roederer, I. U., Lawler, J. E., Sobeck, J. S., et al. 2012, *ApJS*, 203, 27
- Rosswog, S., & Liebendörfer, M. 2003, *MNRAS*, 342, 673
- Rosswog, S., Liebendörfer, M., Thielemann, F., et al. 1999, *A&A*, 341, 499
- Ruffert, M., Janka, H.-T., & Schaefer, G. 1996, *A&A*, 311, 532
- Ruiz, M., Lang, R. N., Paschalidis, V., & Shapiro, S. L. 2016, *ApJL*, 824, L6
- Sądowski, A., Narayan, R., Tchekhovskoy, A., et al. 2015, *MNRAS*, 447, 49
- Sekiguchi, Y., Kiuchi, K., Kyutoku, K., & Shibata, M. 2011, *PhRvL*, 107, 051102
- Sekiguchi, Y., Kiuchi, K., Kyutoku, K., Shibata, M., & Taniguchi, K. 2016, *PhRvD*, 93, 124046
- Shakura, N. I., & Sunyaev, R. A. 1973, *A&A*, 24, 337
- Shappee, B. J., Simon, J. D., Drout, M. R., et al. 2017, *Science*, 358, 1574
- Shibata, M., Fujibayashi, S., Hotokezaka, K., et al. 2017, *PhRvD*, 96, 123012
- Shibata, M., Sekiguchi, Y.-I., & Takahashi, R. 2007, *Prog. Theor. Phys.*, 118, 257
- Shibata, M., & Taniguchi, K. 2006, *PhRvD*, 73, 064027
- Siegel, D. M., Ciolfi, R., Harte, A. I., & Rezzolla, L. 2013, *PhRvD*, 87, 121302
- Siegel, D. M., & Metzger, B. D. 2017, *PhRvL*, 119, 231102
- Siegel, D. M., & Mösta, P. 2018, *GRMHCon2prim: a framework for the recovery of primitive variables in general-relativistic magnetohydrodynamics*, Zenodo, doi:10.5281/zenodo.1213306.
<https://doi.org/10.5281/zenodo.1213306>

- Siegel, D. M., Mösta, P., Desai, D., & Wu, S. 2018, *ApJ*, 859
- Smartt, S. J., Chen, T.-W., Jerkstrand, A., et al. 2017, *Nature*, 551, 75
- Snedden, C., Cowan, J. J., Lawler, J. E., et al. 2003, *ApJ*, 591, 936
- Soares-Santos, M., Holz, D. E., Annis, J., et al. 2017, *ApJL*, 848, L16
- Stergioulas, N. 2011, *International Journal of Modern Physics D*, 20, 1251
- Symbalisty, E., & Schramm, D. N. 1982, *ApJL*, 22, 143
- Tanaka, M., & Hotokezaka, K. 2013, *ApJ*, 775, 113
- Tanaka, M., Utsumi, Y., Mazzali, P. A., et al. 2017, *PASJ*, 69, 102
- Tanvir, N. R., Levan, A. J., González-Fernández, C., et al. 2017, *ApJL*, 848, L27
- the LIGO Scientific Collaboration, & the Virgo Collaboration. 2017, *PhRvL*, 119, 161101. <https://link.aps.org/doi/10.1103/PhysRevLett.119.161101>
- Timmes, F. X., & Arnett, D. 1999, *ApJS*, 125, 277
- Timmes, F. X., & Swesty, F. D. 2000, *ApJS*, 126, 501
- Tóth, G. 2000, *J. Comput. Phys.*, 161, 605
- Valenti, S., David, Sand, J., et al. 2017, *ApJL*, 848, L24
- van Riper, K. A., & Lattimer, J. M. 1981, *ApJ*, 249, 270
- Velikhov, E. P. 1959, *Sov. Phys. JETP*, 36, 995
- Villar, V. A., Guillochon, J., Berger, E., et al. 2017, *ApJL*, 851, L21
- Wollaeger, R. T., Korobkin, O., Fontes, C. J., et al. 2017, *ArXiv e-prints*, arXiv:1705.07084
- Wu, M.-R., Fernández, R., Martínez-Pinedo, G., & Metzger, B. D. 2016, *MNRAS*, 463, 2323